Centrifuge modelling of liquefaction flow slides

S.D.B. Gerlach

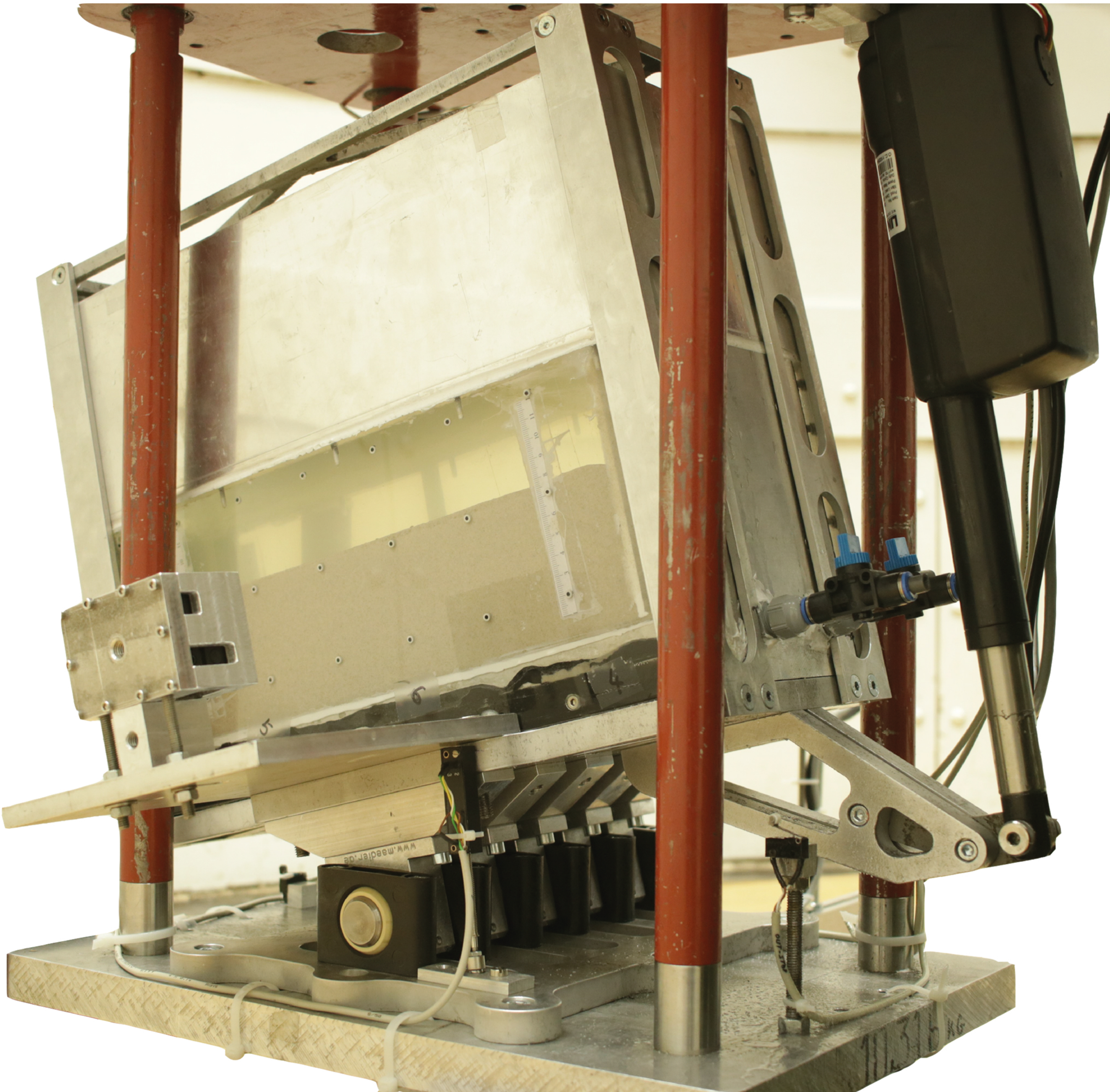

Centrifuge modelling of liquefaction flow slides

by

Simon David Benjamin Gerlach

to obtain the degree of Master of Science
at the Delft University of Technology,
to be defended publicly on Wednesday December 5, 2018 at 10:30 AM.

Student number:	4217101	
Project duration:	December 2017 – December 2018	
Thesis committee:	Dr. Sc. A. Askarinejad	TU Delft, chairman
	Prof. dr. ir. M. A. Hicks	TU Delft
	Dr. ir. M. A. de Schipper	TU Delft
Daily supervisor:	Ir. W. Zhang	TU Delft

TU Delft Delft University of Technology

Preface

About a year ago I joined this project when the newly developed centrifuge set-up was almost finished. The initial research objective was to install a pipe in the sand bed and measure the forces acting on it during liquefaction. The time table turned out to be too optimistic as the centrifuge experiments with the set-up showed many teething problems. The new objective was to investigate until what gravity level and density liquefaction could be triggered. However, the unexpected results showed a totally different outcome and the initial approach was eventually considered unsuccessful. The results nevertheless provided a better understanding of the failure mechanism leading to liquefaction flow slides. I decided to follow an untraditional way of reporting by using a paper format, which – I hope – makes it easier to read and follow the thread through my research. In the end, this thesis shows how important it is to truly understand the mechanics of soil behaviour before setting up an experimental test program.

I want to thank my daily PhD supervisor Weiyuan Zhang for performing all the experiments together and for his feedback on my reports. Additionally, I want to thank my main supervisor Professor Amin Askarinejad for introducing me to this interesting project, and Professors Michael Hicks and Matthieu de Schipper for completing my thesis committee.

I want to express my gratitude to the complete laboratory staff for their rapid help when I needed something, and especially Han de Visser for accompanying us with all the centrifuge experiments we performed. I also want to thank Kees van Beek and Ronald van Leeuwen for their support with the electronic devices.

I am most grateful to my girlfriend Sandra, who had the courage to give up her life in Sweden and move to me. Without her incredible and unconditional support, especially during the most difficult times, I would not have been able to start and finish any Master's program. I also appreciate the presence of our canine family: Grabben, Lassie and Sam. Their untameable enthusiasm gave me a lot of energy, while our daily walks provided me with plenty of time to think about soil behaviour.

I wrote this report in memory of my beloved mother, who was diagnosed with cancer 2.5 years ago and passed away just before I could finalise this thesis. Her perseverance in life and devotion to her children have been my most valuable inspiration.

Simon Gerlach
Delft, November 2018

Centrifuge modelling of liquefaction flow slides

S.D.B. Gerlach

November 28, 2018

Abstract

As soil behaviour is stress-dependent, a centrifuge model with tilting sample box was developed to generate liquefaction flow slides at higher confining stresses. The design and experimental set-up were based on the large liquefaction tank (de Jager et al., 2017). Fluidisation was used as sample preparation technique to produce a saturated, loose and uniform sand bed. The performance of the fluidisation system was evaluated by experimental investigation of the sample by considering the relative density, uniformity, degree of saturation and the influence of viscous pore fluid. The reproducibility of the initial sample was considered acceptable. A series of centrifuge experiments was conducted where the fluidised sand bed was accelerated to varying gravity levels and inclined to a slope with constant tilting rate. In most tests the soil response was characterised by a rapid liquefaction flow slide and a sudden increase in pore pressures. The moment of failure was consistently influenced by a variation in fluid viscosity and tilting rate, regardless of the gravity level; these effects indicated that instability was caused by the restricted seepage rate during loading. It is believed that the liquefaction potential is governed by the extremely loose and highly contractive top layer, which yields a sudden loss of strength under limited drainage conditions. The pore pressure measurements, which showed no excess pore pressures building up prior to failure, can lead to a misunderstanding of the failure mechanism and false assumption of fully drained conditions. Monitoring the pore pressures is therefore not suitable to predict liquefaction flow slides in submarine slopes. Mitigation of liquefaction should be focussed on densification of the looser part of the sandy slope, which is usually the top layer.

1 Introduction

Liquefaction flow slides form a major geohazard for subaqueous slopes as the displacement of enormous liquefied soil volumes can either damage submarine structures or undermine the foundations of coastal assets. In the Netherlands, submarine slides are an important concern as they endanger the coastal structures protecting the country from flooding. More than two hundred flow slides have been recorded during the last centuries (Koppejan et al., 1948; Silvis and de Groot, 1995). Much attention has recently been paid to the Eastern Scheldt storm surge barrier, where scouring due to strong currents undermines the robustness of the barrier foundation (de Groot and Mastbergen, 2006). The toe of the slopes are undercut by erosion which leads to slope instability. Subsequently, a minor triggering mechanism can cause a liquefaction flow slide. Although a large experimental program was carried out prior to construction, the design was based on a situation where no flow slides would occur Rijkswaterstaat (1994). As the scour holes are deeper than expected, is it important to gain a better understanding of the failure mechanism which initiates liquefaction flow slides.

Although element testing in the laboratory is a well-known method to evaluate the liquefaction potential of soils (Jefferies and Been, 2016), it has limitations due to the sample size and imposed drainage conditions. As the initiation of liquefaction is dependent on the geometry and in-situ shear strength, physical modelling is required in the evaluation of soil behaviour and validation of numerical models. Both large scale and centrifuge experiments have been performed to produce liquefaction flow slides (Eckersley, 1990; Phillips and Byrne, 1995; Coulter and Phillips, 2003; Ng, 2008; Gue et al., 2010; de Groot et al., 2012; Beddoe and Take, 2016). To get a better insight of the failure mechanism, a liquefaction tank was developed at Delft University of Technology to induce liquefaction flow slides at large scale (de Jager et al., 2017; de Jager, 2018). The tank contains a submerged sand bed which can be fluidised and tilted to trigger slope failure. As the layer height is limited, the geo-centrifuge can be used to perform a similar experiment with different geometry and higher confining stresses. A centrifuge model with tilting strongbox was developed; the experimental set-up was based on the design of the large liquefaction tank.

The objective of this paper is to present the first experiments conducted with the new centrifuge model. The basic principles of centrifuge modelling are outlined, followed by a description of the experimental set-up in the centrifuge. An experimental investigation of the fluidised sand bed is presented, where the reproducibility of the initial sample is evaluated in terms of relative density, degree of saturation and uniformity. Tilting experiments were performed to trigger liquefaction flow slides at different gravity levels to gain a better understanding of the failure mechanism. The factors which influence the moment of instability and soil response are discussed and analysed. The paper concludes with a discussion, limitations and recommendations for further research.

2 Centrifuge modelling

2.1 Basic principle

Soil models in the centrifuge are subjected to radial acceleration to create a gravity field which is much stronger than the gravity of Earth (g). Centrifuge modelling is used to reproduce the stress level of a corresponding prototype at large scale. The vertical stresses in the centrifuge model and prototype at depths h_m and $h_p = Nh_m$ will be identical, where h_m and h_p are the heights of the model and prototype, respectively. The scaling factor N, which determines the increased gravity field, is related to the acceleration by $Ng = \omega^2 r$, where ω is the angular velocity and r is the radius from the model to the centre of the centrifuge (Figure 1).

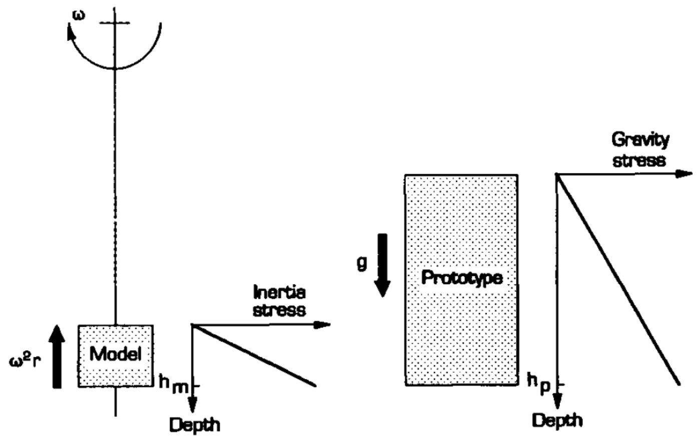

Figure 1: Relationship between the stresses in a centrifuge model and corresponding prototype (Taylor, 1995)

2.2 Scaling laws

The similarity in stress level of model and corresponding prototype requires scaling of other parameters. Garnier et al. (2007) provides a catalogue of scaling laws obtained from centrifuge experiments. The relevant scaling laws, which are obtained by either dimensional analysis or evaluation of governing equations, are listed in Table 1. While the scaling ratio of dimensional variables is straightforward, appropriate scaling of time is more complicated. A distinction is made between dynamic and seepage events, which have a time scale factor of $1 : N$ and $1 : N^2$, respectively (Taylor, 1995). This conflict needs to be considered in liquefaction problems where the generation and dissipation of excess pore pressures play a crucial role. In order to match the time scaling factor of motion and seepage flow, it is suggested to slow down the dissipation rate by increasing the fluid viscosity by a factor of N. A scaling factor of $\sqrt{N}$ for the viscosity was proposed by Askarinejad et al. (2014) when considering static liquefaction problems.

Table 1: Scaling laws

Parameter	Units	Scaling law model/prototype
Gravitational acceleration	m^2/s	N
Length	m	1 / N
Volume	m^3	1 / N^3
Mass	kg	1 / N^3
Stress	N/m^2	1
Strain	-	1
Seepage time (consolidation)	t	1 / N^2
Dynamic time	t	1 / N

2.3 Gravity field effects

When using a gravitational acceleration of Ng, the height of the prototype is equivalent to N times the height of the model and the stress level is supposed to be equal in model and prototype. However, the distribution of vertical stresses is affected by the centrifuge radius resulting in an error of under- and over-stress (Figure 2). This consideration results in a perfect agreement of stresses between model and prototype at two-third of the model's depth. The effective radius is then measured from the axis to one-third the depth of the model (Taylor, 1995). The maximum error is considered negligible for most centrifuges as the ratio between model height and effective radius is small.

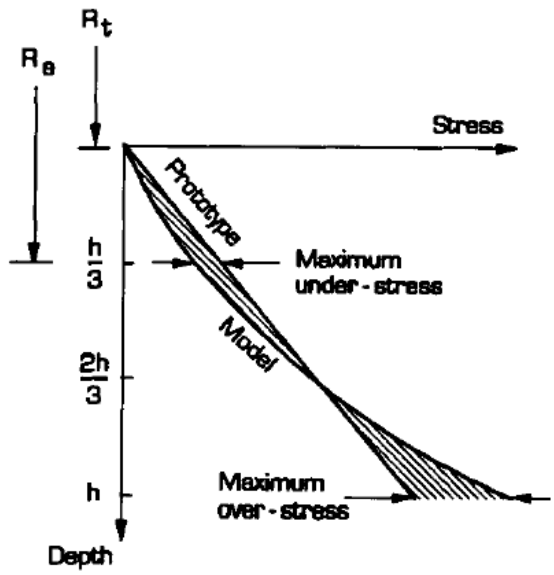

Figure 2: Stress variation with depth in a centrifuge model and corresponding prototype (Taylor, 1995)

2.4 Particle size effects

The question often rises whether the particle size should be scaled down in the centrifuge model. Although theoretically correct, this method is not preferable as scaling the grain size would change the soil type and properties; a clay material would be used in the model to reproduce a sandy soil, resulting in a different soil classification due to the mineralogy and water retention. Consequently, using a clay instead of sand would result in erroneous stress-strain soil behaviour (Madabhushi, 2015). In order to accurately model the soil behaviour during liquefaction, the sand from the prototype should be used in the centrifuge. The argument of not scaling down the particles implicates that the soil is treated as a continuum, which is a generally applied hypothesis in soil mechanics. This assumption is valid if no interacting structure is involved whose dimensions are approaching the particle size.

3 Experimental set-up

3.1 Centrifuge

The geotechnical beamcentrifuge at Delft University of Technology consists of a central spindle with two identical baskets on each side which measure (length x width x height) 40 x 40 x 50 cm. The platform of one basket is used for the soil model while weights are placed on the platform of the other basket to assure balance symmetry. The radius from the centre to the outer side of the basket measures 1.22 m.

3.2 Sample box

The sample box or strongbox designed for the centrifuge experiments consists of a base frame and short walls of aluminium and longer walls of plexiglass. A hollow upperbox made of aluminium is fixed on top to assure a sufficiently high water table during tilting. The outer side of the strongbox measures (length x width x height) 400 x 164 x 130 mm and the upperbox adds another 140 mm to the height. The dimensions were chosen such to create the largest possible model which fits into the centrifuge basket. The inner area of the strongbox measures (length x width) 380 x 134 mm.

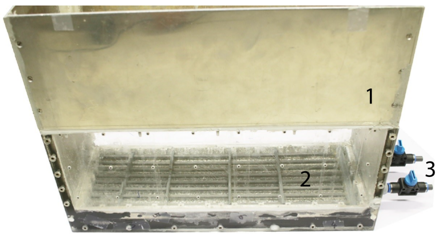

(a) Side view

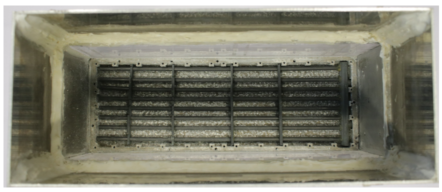
(b) Top view

Figure 3: The strongbox with 1) upperbox; 2) fluidisation frame; 3) valves

3.3 Fluidisation system

The fluidisation system consists of a PVC frame including eight long tubes, connected to a perpendicular thicker tube and two outflow tubes going through the wall (Figure 3). Two valves on the outside are added to this frame to regulate the in- and outflow. The aluminium frame along the boundaries which encloses the fluidisation framework is used to fix a filter on top to prevent sand from clogging the holes. The filter consists of two metal granular plates with different mesh size and a synthetic filter layer in between. Figure 4 shows both sides of the filter, which contains holes to fix the filter to the aluminium frame. In later experiments — which are out of the scope of this report — the holes are used to attach a pipe in various positions.

3.4 Tilting apparatus

An aluminium tilting frame, which holds the strongbox, is installed on the platform of the centrifuge basket (Figure 5). A potentiometer connects the tilting

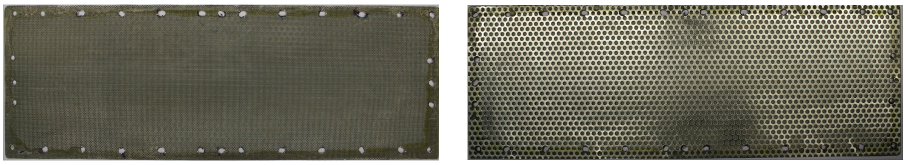

(a) Upper side (b) Lower side

Figure 4: The filter which is placed on top of the fluidisation frame

surface with the base to measure the change in distance and corresponding angle (see Appendix A). The frame is connected to a linear motor (type *Linak*), which is attached to two batteries and a device to control the tilting rate. Microswitches are used as safeguard to stop the motor when the rotating surface reaches the horizontal or final slope position.

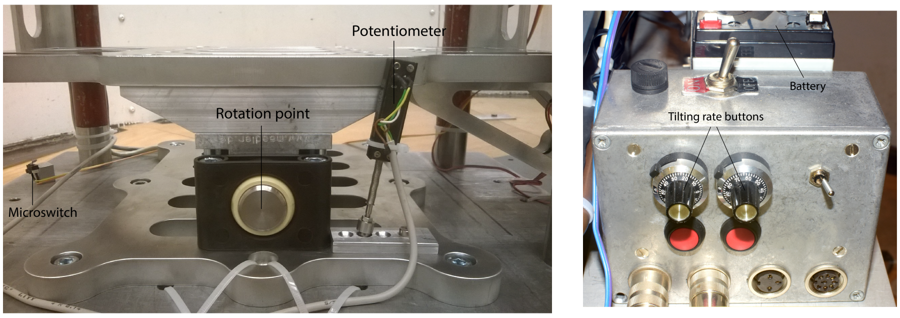

Figure 5: Tilting frame (left) and controller (right)

3.5 Instrumentation

Three calibrated pressure sensors (type *MPXH6400A*) are used as pore pressure transducers (PPTs) and positioned along the length on the bottom of the strongbox (Figure 6). Sensor P3 is placed in the middle with equal distance to the other sensors P1 and P2.

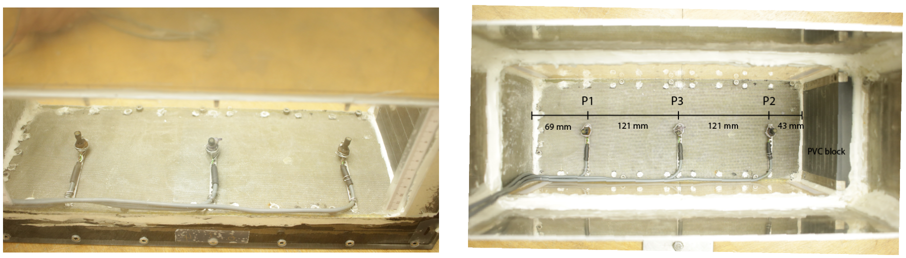

(a) Side view (b) Top view

Figure 6: Positioning of pressure sensors inside the strongbox

The PVC block, which was added to optimise the fluidisation system (see Appendix B), decreases the original inner length to 354 mm. The additional cables are redirected towards the edge and go out on the downhill side of the sand layer in order to minimise the disturbance of a potential slope failure. The sensors are connected to the data acquisition system, which is controlled by *MP3* software. The data logging rate for the readings can be defined with a maximum of 10 samples per second.

Two cameras are installed on each side of the sample box. One high resolution camera (type *DMK*) is fixed to the centrifuge basket and is used to receive live images during flight. The other camera is a *GoPro Hero 4 Black* which is placed in front of the strongbox; it is attached to the tilting surface to move simultaneously with the sample. Figure 7 shows the centrifuge set-up from both sides including the camera positions.

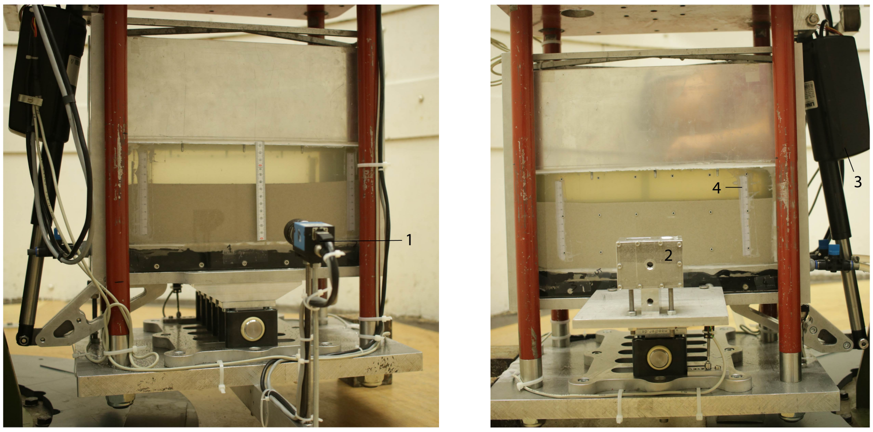

Figure 7: Centrifuge set-up from both sides with 1) high resolution camera; 2) GoPro camera; 3) linear motor; 4) measuring tape

3.6 Soil material

As discussed in Section 2.4, it was preferred to use the soil material from the prototype in the centrifuge model. *Geba* sand was selected to conduct the series of experiments. It is a fine, uniform and subrounded type of sand and therefore sensitive to liquefaction. Table 2 summarises the main soil properties.

Table 2: Soil properties (de Jager et al., 2017; Maghsoudloo et al., 2017)

Property	**Symbol**		**Unit**
Average grain size	D_{50}	0.125	mm
Coefficient of uniformity	D_{60}/D_{10}	1.35	-
Minimum void ratio	e_{min}	0.64	-
Maximum void ratio	e_{max}	1.07	-
Specific gravity	G_s	2.67	-
Hydraulic conductivity	k	4.2E-5	m/s
Residual friction angle	ϕ	35	°

3.7 Viscous fluid

The scaling law of seepage time is examined by decreasing the hydraulic conductivity by increasing the kinematic viscosity of the pore fluid. The viscous fluid is prepared by mixing hydroxypropyl methylcellulose (HPCM) powder with water, together with a small amount of glycerol to improve the homogeneity of the aqueous mixture. The viscosity is measured by a viscometer and is adjusted for various experiments at different gravity levels. Details about preparation and measuring the viscosity are given in Appendix C.

The solution with HPCM is a non-Newtonian, shear-thinning liquid, which means that the viscosity decreases with increasing shear rate. However, Adamidis and Madabhushi (2014) concluded that it can be considered as a Newtonian fluid up to a viscosity of 100 cSt. Dewoolkar et al. (1999) performed triaxial tests with viscous fluid which showed no effect on the constitutive behaviour of sand.

4 Properties fluidised sand bed

Fluidisation is used as sample preparation technique to obtain a homogeneous fully saturated sand bed in loose state. Considering the series of experiments aiming at triggering flow slides in the centrifuge, reproducibility of the initial sample is essential. This section provides experimental investigation of the relative density, degree of saturation and uniformity of the fluidised samples. Additionally, the influence of the fluid viscosity on these properties is evaluated.

4.1 Methodology sample preparation

Water-pluviated sand was initially subjected to vacuum pressure to assure full saturation. Once the saturated sand was transferred to the strongbox, it was kept completely submerged and used for all experiments. Loose samples were prepared by fluidising the sand with de-aired water or viscous fluid (see Appendix D). The fluidisation procedure was characterised by a maximum discharge of 5 l/min during a time span varying between 1.5 and 5 minutes. The duration of fluidisation was affected by several factors such as fluid supply, overflow and the viscosity of the fluid. Manual stirring was applied during fluidisation to loosen the sample and improve the homogeneity of upward flow. When the maximum height of the bed expansion was reached, the flux was continued without stirring while the supply lasted. The fluidisation stage was followed by settlement or resedimentation of the sand until all pore pressures had dissipated; the pressure difference was approximately 0.5 kPa for all tests. Although exact repetition of the fluidisation protocol was difficult, the reproducibility of each initial sample was considered acceptable.

4.2 Relative density

The mass of the dry sand was initially weighted before saturation. The sand which was flushed away during fluidisation, was collected and weighted to back calculate the mass which was left in the strongbox. The measurement tapes on the plexiglass inside the strongbox were used to define the average height of the sand bed. Considering the known area, the volume of the sand bed and consequently the average relative density could be assessed (see Appendix E). The uncertainty in mass resulted in a low accuracy of the calculated density. Taking this error into account, the average relative density of the fluidised samples covered a range of 23–33%.

4.3 Degree of saturation

A simple mass-volume method (Chapuis, 2004) was used to verify the degree of saturation. Four samples were examined after fluidisation to obtain their degree of saturation, as outlined in Appendix F. The results, which include the uncertainty, are listed in Table 3. Although the measured degree of saturation is close to 100%, the limited accuracy of this method cannot assure full saturation of the sand. Other techniques such as the geophysical method with P-wave velocity (Tsukamoto et al., 2002) were examined but considered infeasible due to the design of the strongbox; in that case bender elements would need to be attached on the inner glass side walls.

Table 3: Degree of saturation of four samples

	Sample 1	Sample 2	Sample 3	Sample 4	Average
S_r (%)	99.9 ±1.8	98.7 ±1.7	98.7 ±1.6	99.2 ±1.7	99.1 ±1.7

As full saturation cannot be demonstrated, it is important to consider the implications. Although some authors have evaluated the influence of air on the liquefaction resistance (e.g. Yoshimi et al. (1989); Okamura and Inoue (2012)), such research is usually aimed at undrained tests and dynamic loading conditions. Other investigation with a set-up similar to the fluidisation system showed that fluidisation with fully de-aired water results in an increase of S_r up to 100% (Chapuis, 2004). Additionally, centrifugal acceleration can cause air to be expelled resulting in a higher S_r (Okamura and Inoue, 2012). Considering both factors in combination with the results of measured S_r, full saturation of the sand can be assumed when de-aired supply fluid is used during fluidisation.

4.4 Uniformity

The uniformity of the fluidised sand bed was examined by the macro-CT scanner at Delft University of Technology (Figure 8). This *Siemens Somatom Volume Zoom* CT scanner has a resolution of 0.3 mm, which is not sufficient to distinguish separate grains of the fine Geba sand. However, the obtained CT numbers, which are expressed by the Hounsfield scale, describe the radiodensity of the sand; i.e. the ability of electromagnetic radiation to move through a material. Assuming full saturation of a porous medium, there exists a linear relationship between the Hounsfield Units (HU) and bulk density, which can be used to express the porosity or relative density of the sand (Desrues et al., 1996; Duchesne et al., 2009; Vinegar et al., 1991). Despite the noise caused by the metallic material of the strongbox (filter, PPTs), the uniformity could be analysed by comparing various scans; more details are given in Appendix G.

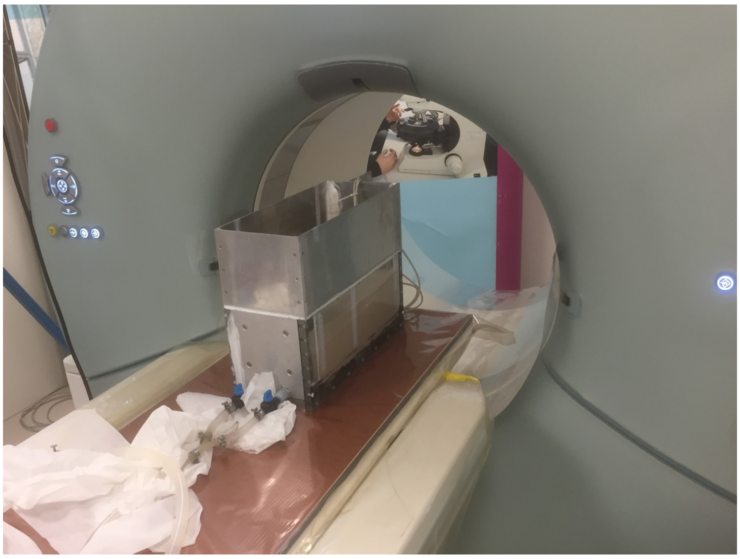

Figure 8: Fluidisation on the table of the CT scanner

Four scans were performed to evaluate the variation of density after fluidisation of the sample. Scanning the entire strongbox required moving the table, which caused a shock and disturbance of the sample. To overcome this problem, the largest possible section (*slice*) of the strongbox without moving the table was scanned before and after fluidisation. Afterwards the table was moved again to observe the difference in relative density caused by the impact. Figure 9 illustrates the 3D view in Hounsfield scale of the scanned strongbox and slice. The scan of the undisturbed slice was used to evaluate the density profiles over the width and depth of the fluidised sample (Figure 10).

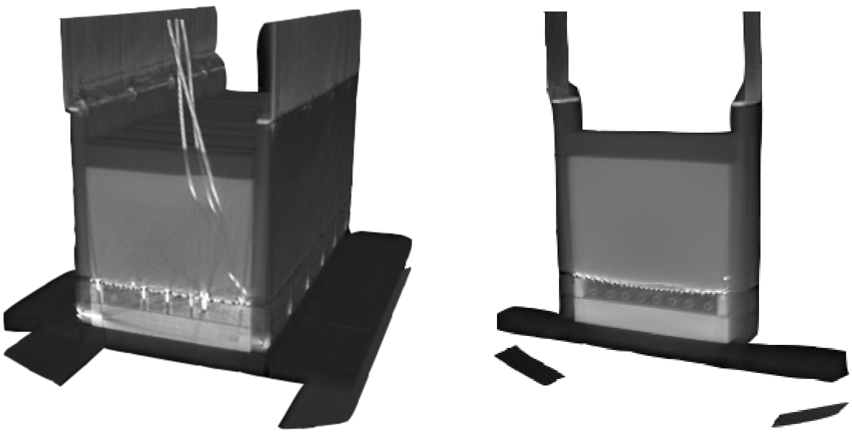

(a) Strongbox

(b) Slice

Figure 9: 3D view of analysed CT scans

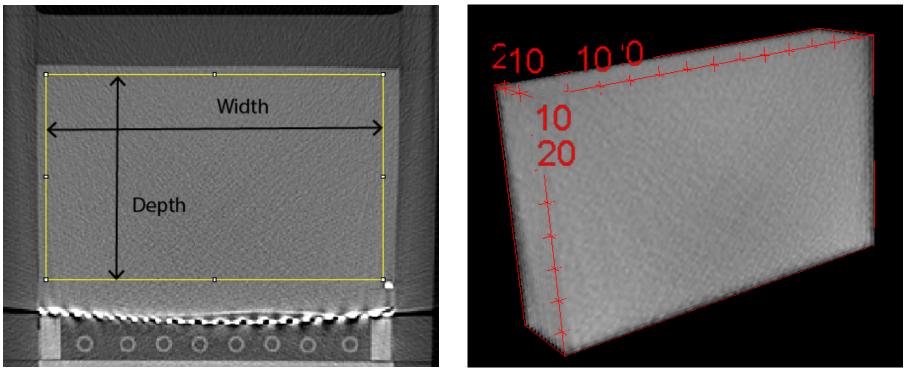

(a) Cross section

(b) 3D view

Figure 10: Undisturbed slice of sand

The variation of relative density (D_r) over the width, which is illustrated in Figure 11, shows a higher value along the boundaries compared to the middle, with a difference of nearly 15%; this dissimilarity is caused by wall friction and a lack of discharge during fluidisation near the long boundaries. An error band is included to indicate the uncertainty, which is higher at the boundaries due to the reflections of the metallic material.

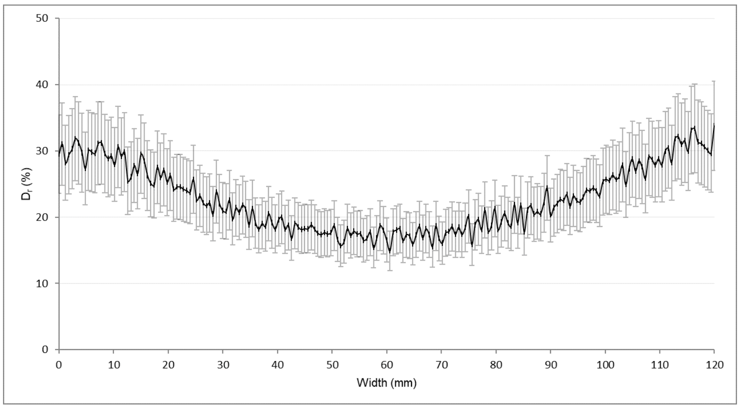

Figure 11: Variation in relative density along the width

Figure 12 shows the relative density variation over the depth, which is characterised by an extremely loose top layer of 20 mm with a downwards increasing relative density of approximately 25%, followed by a layer of 40 mm with constant relative density and a bottom layer of 20 mm with an increase in relative density up to 50%. It is believed that the large rise of density at the bottom is caused by an insufficient upward flow; the maximum increase in pore pressure during fluidisation was approximately 0.5 kPa, while the effective stress was 0.7 kPa. As the applied flow was calculated to be sufficient, it could be due to the presence of sensors and cables at the bottom of the strongbox. It should be mentioned that the exact magnitude of this increase is uncertain due to reflections of the metallic filter. An error band is added to indicate the uncertainty.

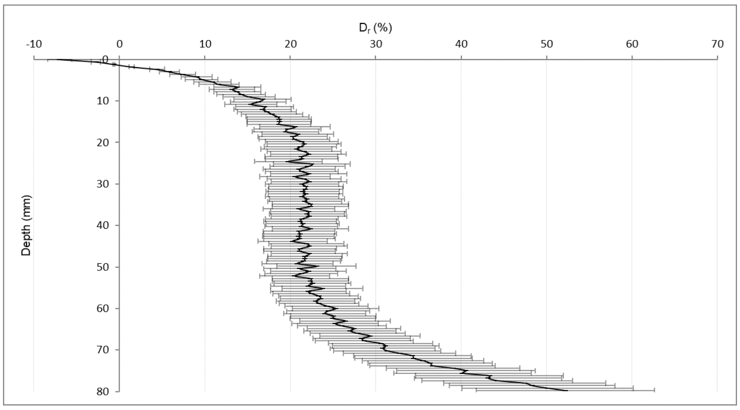

Figure 12: Variation in relative density along the depth

Figure 13 illustrates the cross sections of the total strongbox with the sample which was affected by movement of the table. A sharp transition of the upper and lower layer can be observed; it is assumed that the sudden shear deformation caused by the shock provoked excess pore pressures resulting in liquefaction and densification of the top layer. However, comparing similar cross sections before and after disturbance showed that the relative density of the lower part is hardly affected (see Appendix G). Analysing the lower area gives an indication of the relative density profile over the total length (Figure 14). Ignoring the artefacts caused by the reflections of PPTs and cables, a uniform trend in relative density over the length with a fluctuation of 5% can be observed. No error band is added as the reflections are similar for each cross section.

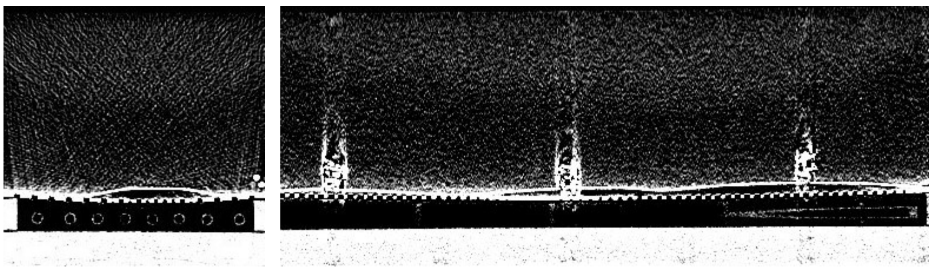

(a) Width (b) Length

Figure 13: Cross sections of the sample disturbed by movement of the CT table

Lamens (2015) investigated the uniformity of permeability and particle segregation of fluidised Geba sand in a permeameter. The sand column showed an increase of mean particle size from top to bottom; the grain size of the fines on top was almost twice as small as the grains near the bottom. The permeability increased linearly downwards, which implied that the particle segregation has a bigger influence on the permeability than the porosity, and the permeability at the top is lower due to the higher fine content. Although it was not feasible to investigate these properties in the strongbox, it is reasonable to assume similar conditions of the fluidised sand bed. Fluidisation results in a particle segregation with fines on top, from which a certain amount is flushed away during preparation of the sample.

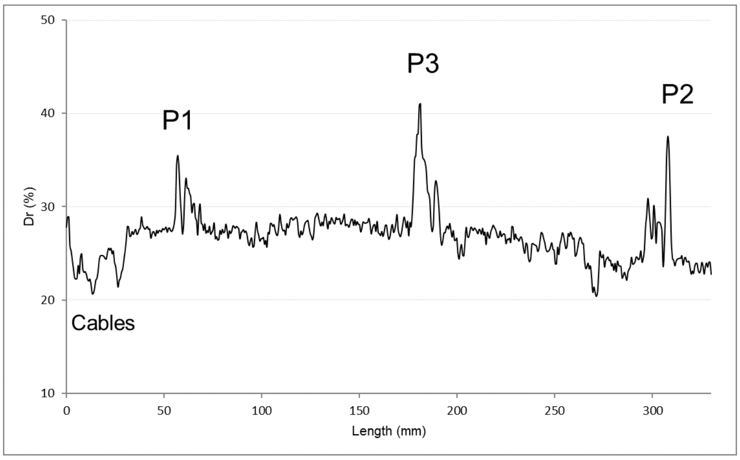

Figure 14: Variation in density along the length (lower part)

4.5 Influence of viscous fluid

Sample preparation with viscous fluid is similar to the procedure with water. One difference is the reuse of the viscous fluid, as the supply is limited in contrast to water. The drained fluid was collected in a container, filtered from sand particles, and used again. Vacuum saturation was applied to the fluid after three experiments. Although the degree of saturation with viscous fluid was not investigated, recycling the fluid showed no influence on the sand behaviour.

The settlement time after fluidisation increased with higher viscosities of pore fluid. However, the viscosity had no influence on the obtained height and average relative density of the sand bed when fully settled. It is therefore assumed that the variation in density over the width, length and height is comparable to the sand bed which was investigated with water as pore fluid. It is concluded that the fluidisation system works properly with viscous fluid.

5 Tilting experiments

Due to the complexity of the experimental set-up and unexpected results, the planned testing program was adjusted throughout the project. Initially, the main objective was to evaluate until what gravity level and corresponding average relative density of the sample a liquefaction flow slide could be produced. Analysis of the results showed that relating the density to liquefaction potential was too simplistic as other factors such as tilting rate, fluid viscosity and disturbance played a crucial role. Nevertheless, the results provided insight into the failure mechanism and the appropriate scaling law to simulate the corresponding prototype. This section describes the testing procedure and provides an overview of the performed tilting experiments. The response of the PPTs during the experiment and the observed liquefaction flow slide are evaluated.

The results are interpreted by means of the failure angle, and several factors influencing the soil behaviour are being discussed.

5.1 Testing procedure

The initial sample for each tilting test was prepared inside the centrifuge basket by fluidisation, as described in Section 4. The average height was determined by the measurement tapes when settlement had finished. The GoPro camera started recording just before the centrifuge was turned on to capture the total experiment. The centrifuge was accelerated to the required gravity level with a rate of 0.1 RPM/s, corresponding to a time span of approximately 40 minutes to go from 1g to 50g. When arriving at the intended gravity level, tilting was started after 90–120 seconds. The strongbox inside the frame was tilted with specified rate to the steepest inclination of approximately 20°, no matter if any flow slide was observed. The strongbox was either tilted back (at lower gravity levels) or remained in the slope position while the centrifugal acceleration was brought back to zero.

Table 4: Overview of tilting experiments in the centrifuge

Test name	g-level (N)	Viscosity (cSt)	Tilting rate (°/s)
V03	10	3	0.1
V04		3	2.0
V05		3	1.0
V06		3	0.5
V07		3	0.1
V08		9	0.1
V09		8	0.1
V10	30	6	2.0
V11		6	0.1
V12		6	0.1
V18		30	0.1
V19		30	0.1
V15	50	7	0.1
V16		7	0.1
V17		7	0.1
V20		50	0.1
V21		50	0.1

5.2 Overview of experiments

Preliminary experiments with water at different gravity levels were mainly performed to test the set-up and procedure. After some adjustments to optimise the testing protocol, the main series of tests with viscous fluid was carried out. Pore fluids with different viscosities corresponding to a scaling factor of $\sqrt{N}$ and N were used at 10g, 30g and 50g in order to evaluate the proper scaling law for the initiation of liquefaction. Tilting rates of 0.1, 0.5, 1.0 and 2.0°/s were used at 10g to assess the effect of the loading rate. Several tests were performed twice to examine the reproducibility of the experiments. Table 4 gives an overview of the tilting experiments which are used for analysis of the results. It should be noted that the measured viscosity can slightly differ from the intended scaling factor. A detailed overview of all analysed tilting tests can be found in Appendix H.

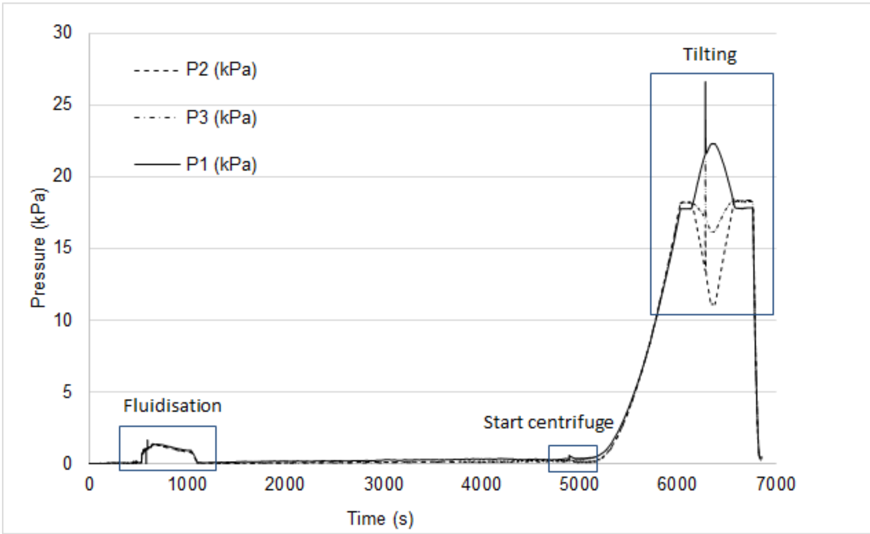

(a) Total duration experiment

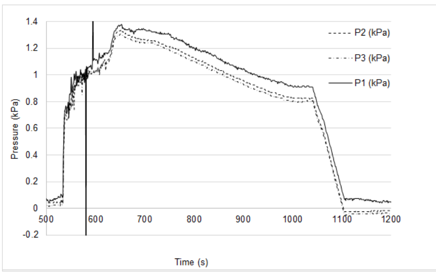

(b) Fluidisation

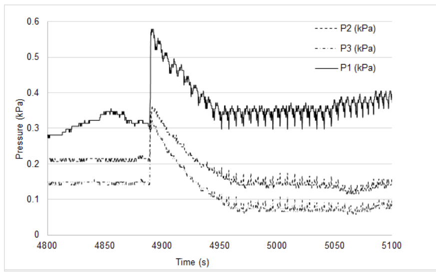

(c) Start centrifuge

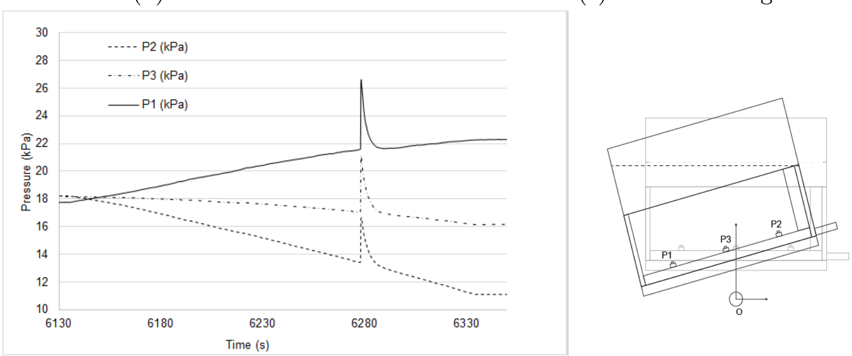

(d) Tilting

Figure 15: PPT response during different stages of centrifuge experiment

5.3 Response of PPTs

The typical response of the pressure sensors was similar for all centrifuge experiments. Figure 15 shows the PPT measurement over time of test V08, indicating the stages of fluidisation, start of the centrifuge and tilting. During fluidisation, the sensors show a rapid increase when initiating the upward flow. The movement and peak during further increase to the highest pressure is caused by manual stirring of the sample. When the discharge is blocked, sedimentation occurs and excess pore pressures dissipate. The pressures flatten to a constant value, which indicates the end of consolidation. Subsequently, the water table is lowered to a level of 18 cm to prevent overflow during tilting.

The start of the centrifuge causes a sudden pressure elevation and the succeeding oscillations are due to the spinning of the centrifuge. The following increase in pressure corresponds to the acceleration of the centrifuge. When the required g-level is reached, the pressures become constant indicating hydrostatic conditions. The gradual change in pressure during tilting is related to the position of the water table and location of the PPTs, as illustrated in the schematic view of the strongbox. At a certain angle a peak is observed, which corresponds to a liquefaction flow slide in the sand bed. After this slope failure, the excess pore pressures dissipate rapidly and the incremental pressures follow the same trend as before until the end of tilting.

5.4 Description liquefaction flow slide

The mechanism of failure is comparable for all experiments, although the duration of the flow slide decreases with increasing gravity level. During tilting only small deformations in the sand bed can be observed before the slide; then a sudden movement of the sand bed is visible which occurs within a few seconds. Figure 16 shows a montage[1] of two following frames just before and after the flow slide of test V08. The colour tints and added lines indicate the difference of the sand surface when comparing the images.

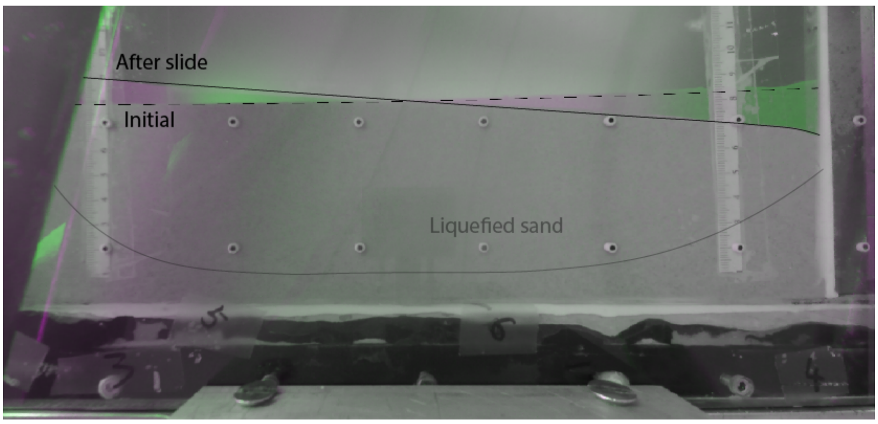

Figure 16: Surface of the sand bed before and after failure

[1]The montage of two GoPro images is created by *MATLAB*, see Appendix O

It can be observed that the slope after failure is slightly more gentle than before. The limited displacement of the liquefied sand is a consequence of the high dissipation rate of excess pore pressures in the centrifuge. The seepage time is N^2 times higher in the centrifuge; hence, the sand quickly regains strength before it flows towards a horizontal position. For test V08, a kinematic viscosity of 9 cSt was used at 10g, which means that the duration of the flow slide is another 10 times smaller than in the prototype: 15 seconds instead of 150 seconds. The lowest line indicates until what depth large movements of the grains can be observed; it is assumed that the sand above this line liquefies while the sand at the bottom remains stable. The circular shape of this transition is supposed to be an effect of the boundaries as the liquefied sand can not move in longitudinal direction.

Since the flow slide occurs very rapidly at higher gravity conditions, frames were taken for a 1g test with a fluid viscosity of 4 cSt (test V02 in Appendix H). They reveal an increasing rate of shear deformation before failure. The magnitude of displacements decrease from top to bottom, corresponding to the vertical density variation of the sample. At the initiation of failure, the frames show a sudden large deformation of the top layer, as if it collapses. The following frame shows large movement of the entire sand bed, implying that the large plastic strains and the corresponding generation of excess pore pressures at the top induced liquefaction at larger depths. The sand, which flows from the crest to the toe, stabilises stepwise from bottom to top while the excess pore pressures dissipate. Subsequently, the grains at the top move furthest whereas the material at the bottom shows minor displacements.

5.5 Influencing factors on soil response

The results of the centrifuge experiments showed that the soil response is influenced by several factors such as fluid viscosity, tilting rate, density and disturbance of the sample. In most tilting tests a liquefaction flow slide was observed, while the sand bed remained stable in a few cases. The effect of influencing factors is investigated by considering the PPT measurements and the moment of failure, which is expressed in terms of failure angle.

Effect of tilting rate

Figure 17 shows the relationship between the tilting rate and failure angle, obtained from the tests at 10g with similar viscosities (V04 to V07). There is a significant drop in failure angle when the rate is increased from 0.1 to 0.5°/s but higher rates have less effect on the failure angle. Increasing the loading rate leads to a higher strain rate and generation of excess pore pressures; as the limited dissipation rate remains unchanged, the time to failure will decrease. When considering the time to failure rather than the angle, the time doubles when the tilting rate is doubled from 0.5 to 1.0 and from 1.0 to 2.0 °/s. The larger difference at lower rates can be explained by the decrease of void ratio due to shear strains prior to failure; hence, the effective stresses are higher and a larger generation of excess pore pressures is needed to cause liquefaction. Wanatowski and Chu (2012) obtained a similar logarithmic relationship between the reduction rate of effective stress and time to instability; the measured axial deformations prior to instability increased with decreasing reduction rate. It should be noted that the onset of instability and sudden loss of strength is a consequence of limited drainage conditions, and the terminology of 'instability under drained conditions' can be confusing.

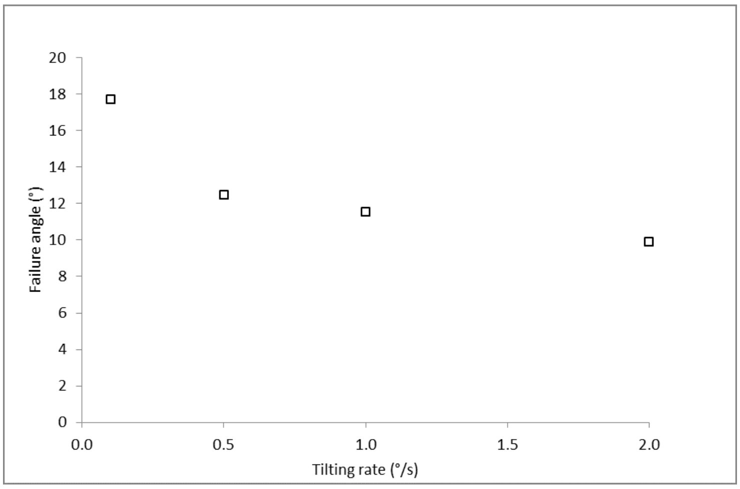

Figure 17: Relationship between tilting rate and failure angle

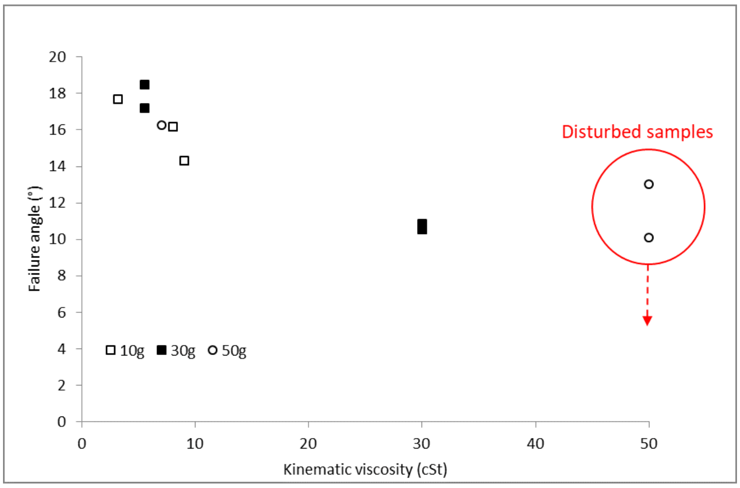

Figure 18: Relationship between viscosity and failure angle

Effect of viscosity

Comparing the tests with different viscosities at a similar tilting rate of 0.1°/s shows a clear trend of decreasing failure angle when increasing the viscosity (Figure 18). The lower failure angle is simply a consequence of the decreasing dissipation rate with higher viscosities. The failure angle is not influenced by the gravity factor N, because both the generation and dissipation of excess pore pressures increase with a factor of N^2 when the same loading rate is applied. In other words, the moment of failure is related to the drainage conditions which depend on the consolidation rate (see Appendix I). With equal model height and loading rate, the moment of failure is solely controlled by the consolidation coefficient of the soil. Decreasing the hydraulic conductivity by increasing the viscosity consequently results in a lower failure angle. It should be mentioned that the tests with a viscosity of 50 cSt were highly disturbed during acceleration (see Appendix J), leading to a higher failure angle than predicted.

Effect of density

The influence of density can be evaluated by comparing repeated experiments. Unfortunately, the initial sample was highly disturbed at the start of the centrifuge, resulting in liquefaction and densification of the top layer (see Appendix K). Due to the density variation over the depth, the effect of average density on the failure angle cannot be determined independently. By quantifying the disturbance at the centrifuge start in terms of pore pressure ratio, a difference in soil response can be observed. Table 5 presents the analysed tests with corresponding relative density before tilting ($D_{r,Ng}$) and the pore pressure ratio at the centrifuge start ($r_{u,start}$), which was assessed from the PPT measurements.

Table 5: Tests used for analysis of density and disturbance

Test name	g-level (N)	$D_{r,Ng}$ (%)	$r_{u,start}$
V03	10	47	0.32
V07		34	0.08
V15	50	52	0.45
V16		49	0.18
V17		49	0.34

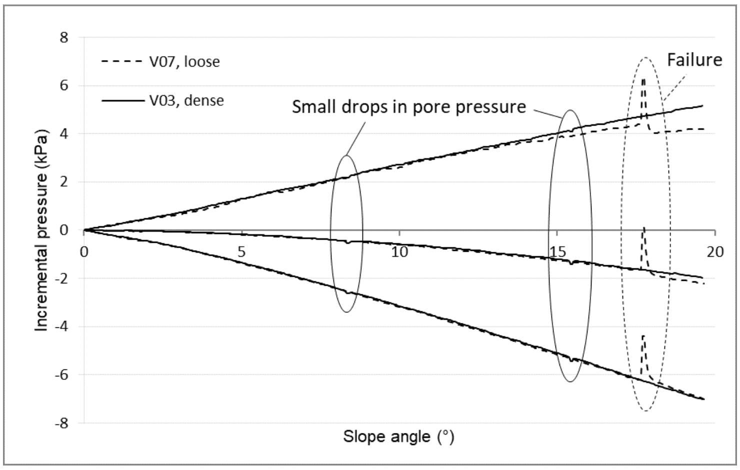

Figure 19: PPT response during tilting of repeated tests at 10g

Figure 19 shows the incremental pressures during tilting of tests V03 and V07. The pressures of test V03 show two smalls drops and no failure was observed, whereas sample V07 failed at an angle of 17.7°, coinciding with a peak in pressure. It is believed that both samples became unstable due to an insufficient seepage rate during shear deformations. However, sample V03 was denser which led to dilative response in undrained conditions, and the negative excess pore pressures resulted in an increase of strength and stabilisation of the sand bed. Sample V07 was looser and the contractive response resulted in an increase of excess pore pressures and loss of strength, with liquefaction as consequence.

Figure 20 shows the PPT response during tilting of the repeated tests at 50g (V15 to V17). Despite the comparable densities, a flow slide was solely observed in test V16 while the other two slopes remained stable. The only difference between the samples was the magnitude of disturbance, which affected the density profile over the depth. This implies that the liquefaction potential is governed by the looser part in the sample, which is the top layer.

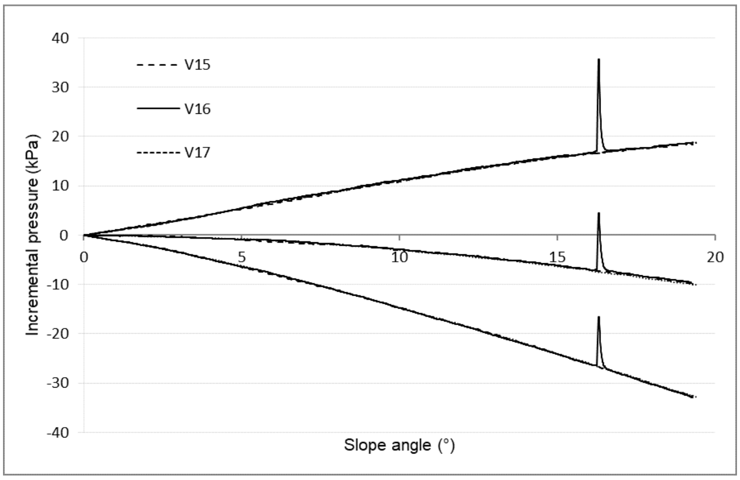

Figure 20: PPT response during tilting of repeated tests at 50g

Gravity and model boundary effects

As described in Section 2.3, the centrifuge model is subjected to a variation in gravity field. The maximum error caused by the variation of stress level with depth is equal to 1.9% during acceleration and increases to 4.0% when the sample box is fully tilted (see Appendix L). Apart from the variation in gravity field over the depth, the fixed centre of rotation causes a variation of radius in the horizontal plane. Consequently, the gravitational field contours form a curvature along the width of the sample., resulting in an error of 0.2%. Another consequence of a rotational acceleration field is the Coriolis effect, which influences the soil movement in the plane of rotation. In order to avoid this problem, the strongbox was designed to be tilted in radial direction, i.e. perpendicular to the plane of rotation. As the velocity of moving particles is low, the Coriolis effect is considered negligible. Table 6 summarises the calculated errors due to gravity effects; it is considered acceptable to neglect the errors as the percentages are low and no effect was observed.

Table 6: Errors due to variation in gravity field

Gravity effect	Maximum error
Stress variation over depth, horizontal strongbox	1.9%
Stress variation over depth, tilted strongbox	4.0%
Radial gravity variation	0.2%
Coriolis acceleration	Negligible

As mentioned before, the closed boundaries influence the drainage conditions as seepage is limited to the upward direction. However, it is unclear whether the side boundaries have a significant influence on the stress-strain behaviour of the sand bed, and if the slope can be analysed as 'infinite'. From the recorded videos, it can be observed that the displacements increase towards the crest of the slope, while they are prevented by the side wall of the toe. Moreover, the increasing strain rate is dominant near the crest, which can be a result of decreasing lateral stresses due to the side wall. Further research is needed to determine the effect of the vertical boundaries.

Effect of sensors

To determine the influence of the sensors and cables in the sand bed, experiment V11 was repeated without any sensors or cables inside the sand layer. The video showed a similar failure mechanism at an angle which was slightly lower, approximately 16°instead of 17.2°. The depth of liquefying sand appeared to be larger as movement along the bottom was visible. It is therefore concluded that the sensors and cables rather decrease the liquefaction potential than triggering any failure. The sensors and cables at the bottom seem to act as a dense reinforcement which prevents liquefaction of the sand; this explains why the movement of flowing sand is limited to 1–2 cm above the bottom. Anyhow, the failure mechanism itself is not effected.

5.6 Concluding remarks

Figures 19 and 20 illustrate that incremental pore pressures up to failure are matching, which indicates that a liquefaction flow slide cannot be predicted by monitoring the pore pressures. This observation supports the hypothesis that the failure is initiated at the top where the density and effective stresses are lowest. Only a small increase in excess pore pressure generation due to an increasing shear rate can be enough to cause sudden instability, as the drainage conditions are limited. Once in undrained conditions, the sand quickly looses its strength (strain softening), resulting in large plastic strains, a sudden accumulation of excess pore pressures and consequently liquefaction of the sand.

In general, the results of the tilting experiments showed that the liquefaction potential depends both on the consolidation rate and density of the sample. When the loading rate and corresponding strains are exceeding the limited dissipation rate, instability can occur. Whether this will evolve into a liquefaction flow slide depends on the density of the sand. Once in undrained conditions, highly contractive behaviour results in large (positive) excess pore pressures; the corresponding decrease in effective stress leads to a loss of strength and liquefaction. If the sand is dense enough showing dilative response, negative excess pore pressures increase the effective stress and the slope will stabilise itself. This mechanism implies that the failure angle in the tilting experiments is dependent on the hydraulic conductivity (viscosity), height, compressibility and density of the sand bed. Additionally, this insinuates that the average density is no adequate measure to predict the moment of instability, as it will increase with increasing layer height, while the failure angle will decrease.

Performing experiments with similar model heights was a flaw in the test plan, as the results give no definite answer on the scaling law compared to the prototype. However, if the purpose is to obtain the same moment of failure in model and prototype, is it clear that the dissipation time of excess pore pressures should be equalised in model and prototype. This can be done by using the same tilting rate and a fluid viscosity which is N^2 higher to overcome the discrepancy in seepage time. Another option is to increase the fluid viscosity by a factor N to match the loading and seepage time, and to apply the same load N times faster in the model; i.e. increasing the loading rate by a factor of N.

Conclusions

Fluidisation in the strongbox yields a uniform sand bed in longitudinal direction, while the density profile over the width varies with loosest state in the middle and increasing density towards the boundaries. The vertical density variation reveals a non-linear decrease over the depth where the top and bottom layers are looser and denser, respectively, with constant density in between. The obtained average relative density of a fluidised sample with height 8–9 cm lies in the range of 23–33%. Assuming full saturation is considered acceptable when the sand is fluidised with de-aired fluid. Increasing the viscosity of pore fluid has no influence on the average density of the sand bed; it is therefore believed that the effect of viscosity on the uniformity and degree of saturation is negligible. In summary, the reproducibility of the initial sample by fluidisation is considered acceptable.

The centrifuge set-up with a tilting sand bed is suitable to produce liquefaction flow slides. The moment of failure depends on the consolidation rate in conjunction with the density of the sand. Increasing the viscosity and tilting rate results in a lower failure angle, while higher densities show a diminishing effect on the liquefaction potential. Recorded frames show a sudden collapse at the top layer before the entire sand bed liquefies; it is therefore believed that liquefaction is a consequence of instability in the extremely loose top layer, which yields a sudden loss of strength (strain softening) and consequently large plastic strains when drainage is limited. This mechanism implies that the moment of failure should be determined by considering the consolidation rate rather than the slope angle. The PPT measurements, which show no excess pore pressures building up prior to failure, can be confusing, leading to the false assumption of fully drained conditions and conclusion that limited drainage conditions cannot be the cause of instability.

Considering the practical implications concerning flow slides near the Eastern Scheldt, liquefaction can be triggered in loose sand regardless of the slope inclination. Monitoring the pore pressures inside the sand layer is not sufficient as instability can occur rapidly without any sign of excess pore pressures prior to failure. Flow slides are likely to be initiated at the top where the sand is loosest due to upward flow and settlement. Liquefaction should be prevented by densification of the top layer; the soil will then show dilative response under limited drainage conditions, resulting in re-stabilisation of the slope.

Limitations and recommendations

As the liquefaction response is governed by the loosest part, and due to the disturbed variation of density in the sand, it was shown that the average relative density was no adequate measure to quantify the liquefaction potential of the tilting sand bed. Since the density nevertheless plays a crucial role in the soil response, the density should be monitored more accurately to determine the critical value for which the sand is susceptible to liquefaction.

Following the scaling law for consolidation, the seepage time in the model is supposed to be N^2 faster compared to the corresponding prototype. Although the order of magnitude regarding the dissipation time of excess pore pressures after the flow slide was reasonable in the experiments, the results were not sufficient to confirm the appropriate scaling factor. The technique *Modelling of models* should be used to verify the scaling law by simulating a certain prototype with different model heights and appropriate fluid viscosity (Madabhushi, 2015).

Observations by eye were used to analyse the movement in the sand bed during settlement and failure. Particle image velocimetry (PIV) should be used to determine the displacement of sand grains (White et al., 2003). This technique will allow to clarify the soil deformation prior to and during liquefaction flow slides in the tilting experiments.

References

Adamidis, O. and Madabhushi, S. (2014). On preparation of viscous pore fluids for dynamic centrifuge modelling. *International Journal of Physical Modelling in Geotechnics*, 15(3):141–149.

Allen, J. (1984). *Sedimentary structures, their character and physical basis.* Eslevier.

Askarinejad, A. (2013). *Failure mechanisms in unsaturated silty sand slopes triggered by rainfall.* PhD thesis, ETH Zrich.

Askarinejad, A., Beck, A., and Springman, S. (2014). Scaling law of static liquefaction mechanism in geocentrifuge and corresponding hydromechanical characterization of an unsaturated silty sand having a viscous pore fluid. *Canadian Geotechnical Journal*, 52(6):708–720.

Beddoe, R. and Take, W. (2016). Loss of slope support due to base liquefaction: comparison of 1g and centrifuge landslide flume experiments. *Soil and Foundations*, 56(2):251–264.

Boorder, M. D. and van der Zon, J. (2017). Triggering of static liquefaction in geo-centrifuge modelling. Bachelor thesis, Delft University of Technology.

Casagrande, A. (1936). Characteristics of cohesionless soils affecting the stability of earth fills. *Journal of Boston Society of Civil Engineers*, 23:257–276.

Chapuis, R. (2004). Permeability tests in rigid-wall permeameters: Determining the degree of saturation, its evolution, and its influence of test results. *Geotechnical Testing Journal*, 27(3):304–313.

Choi, S., Lee, M., Choo, H., Tumay, M., and Lee, W. (2010). Preparation of a large size granular specimen using a rainer system with a porous plate. *Geotechnical Testing Journal*, 33(1).

Chu, J., Leroueil, S., and Leong, W. (2003). Unstable behaviour of sand and its implication for slope instability. *Canadian Geotechnical Journal*, 40(5):873–885.

Coulter, S. (2005). Seismic initiation of submarine slope failures using physical modeling in a geotechnical centrifuge.

Coulter, S. and Phillips, R. (2003). Simulating submarine slope instability initiation using centrifuge model testing. In Locat, J., Meinert, J., and Boisvert, L., editors, *Submarine Mass Movements and Their Consequences. Advances in Natural and Technological Hazards Research*, volume 19. Springer, Dordrecht, the Netherlands.

Davidson, J., Clift, R., and Harrison, D. (1985). *Fluidization.* Academic Press, London.

Davidson, J. and Harrison, D. (1963). Fluidized particles.

de Groot, M., Lindenberg, J., Mastbergen, D., and den Ham, G. V. (2012). Large scale sand liquefaction flow slide tests revisited. Eurofuge, Delft.

de Groot, M. and Mastbergen, D. (2006). Scour hole slope instability in sandy soil. In *International Conference on Scour and Erosion*, Amsterdam, the Netherlands.

de Jager, R. (2018). *Assessing Liquefaction Flow Slides: Beyond Empiricism.* PhD thesis, Delft University of Technology.

de Jager, R., Maghsoudloo, A., Askarinejad, A., and Molenkamp, F. (2017). Preliminary results of instrumented laboratory flow slides. *Procedia Engineering*, 175:212–219.

de Jager, R. and Molenkamp, F. (2012). Fluidization system for liquefaction tank. In *Proceedings of Eurofuge.* Delft University of Technology and Deltares.

Desrues, J., Chambon, R., Mokni, M., and Mazerolle, F. (1996). Void ratio evolution inside shear bands in triaxial sand specimens studied by computed tomography. *Gotechnique*, 46(3):529–546.

Dewoolkar, M., Ko, H., Stadler, A., and Astaneh, S. (1999). A substitute pore fluid for seismic centrifuge modeling. *Geotechnical Testing Journal*, 22(3):196–210.

Duchesne, M. J., Moore, F., Long, B. F., and Labrie, J. (2009). A rapid method for converting medical computed tomography scanner topogram attenuation scale to hounsfield unit scale and to obtain relative density values. *Engineering Geology*, 103(3):100 – 105. Applications of X-ray Computed Tomography in Engineering Geology.

Eckersley, J. (1990). Instrumented laboratory flowslides. *Gotechnique*, 40(3):489–502.

Garnier, J., Gaudin, C., Springman, S., Culligan, P., Goodings, D., Konig, D., Kutter, B., Phillips, R., Randolph, M., and Thorel, L. (2007). Catalogue of scaling laws and similitude questions in geotechnical centrifuge modelling. *International Journal of Physical Modelling in Geotechnics*, 7(3):1–23.

Gue, C., Bolton, M., and Thusyanthan, I. (2010). Centrifuge modelling of submarine landslide flows. In Springman, S., Laude, J., and Seward, L., editors, *Proceedings 7th International Conference on Physical Modelling in Geotechnics, ICPMG 2010*, pages 1113–1118, Zurich. Taylor and Francis.

Hampton, M., Lee, H., and Locat, J. (1996). Submarine landslides. *Reviews of Geophysics*, 34:33–59.

Han, B., Wang, Z., Zhao, H., Jing, H., and Wu, Z. (2012). Strain-based design for buried pipelines subjected to landslides. *Petroleum Science*, 9(2):236–241.

Huang, B., Liu, J., Lin, P., and Ling, D. (2014). Uplifting behavior of shallow buried pipe in liquefiable soil by dynamic centrifuge test. *The Scientific World Journal*, 2014.

Jafarzadesh, F., Jahromi, H. F., Yoosefi, S., Sehizadeh, M., Joshaghani, M., and Alavi, M. (2012). Dynamic response of buried gas pipelines due to earthquake induced landslides by nonlinear numerical modeling. In *Proceedings of the 15th World Conference on Earthquake Engineering*, Lisbon, Portugal.

Jefferies, M. (2017). Soil liquefaction - a mechanics view. unknown publisher.

Jefferies, M. and Been, K. (2016). *Soil Liquefaction: A Critical State Approach*. CRC Press, second edition.

Jefferies, M., Been, K., and Olivera, R. (2012). Discussion of evaluation of static liquefaction potential of silty sand slopes. *Canadian Geotechnical Journal*, 48(2):247–264.

Jommi, C. (2016). Lecture slides in aes1730: Introduction to geotechnical engineering.

Kim, S., Hwang, J., Kim, M., Bao, Y., and Ko, H. (2006). Comparison of 1-g and centrifuge model tests for liquified sands. In *Physical modelling in geotechnics: 6th ICPMG '06*, pages 1319–1324. Taylor & Francis.

Koppejan, A., van Wamelen, B., and Weinberg, L. (1948). Coastal flow slides in the dutch province of zeeland. In *Proceedings of the Second International Conference on Soil Mechanics and Foundation Engineering*, volume V, pages 89–96, Rotterdam, the Netherlands.

Kramer, S. (1988). Triggering of liquefaction flow slides in coastal soil deposits. *Engineering Geology*, 26(1):17–31.

Kramer, S. and Seed, H. (1988). Initiation of soil liquefaction under static loading conditions. *Journal of Geotechnical Engineering*, 114(1):412–430.

Krapfenbauer, C. (2016). Experimental investigation of static liquefaction in submarine slopes.

Kuerbis, R. and Vaid, Y. (1988). Sand sample preparation – the slurry deposition method. *Soils and Foundations*, 28(4):107–118.

Lade, P. (1992). Static instability and liquefaction of loose fine sandy slopes. *Journal of Geotechnical Engineering*, 118(1):51–71.

Lade, P. (2012). Reply to the discussion by jefferies, been and olivera on "evaluation of static liquefaction potential of silty sand slopes". *Canadian Geotechnical Journal*, 49(6):746–750.

Lade, P. and Pradel, D. (1990). Instability and plastic flow of soils. i: Experimental observations. *Journal of Engineering Mechanics*, 116(12):2173–2191.

Lade, P., Yamamuro, J., and Bopp, P. (1996). Significance of particle crushing in granular materials. *Journal of Geotechnical Engineering*, 112(4):309–316.

Lamens, P. (2015). Fluidization before liquefaction: A study of sand bed uniformity. Bachelor thesis, Delft University of Technology.

Madabhushi, G. (2015). *Centrifuge Modelling for Civil Engineers*. CRC Press, London.

Maghsoudloo, A., Galavi, V., Hicks, M., and Askarinejad, A. (2017). Finite element simulation of static liquefaction of submerged sand slopes using a multilaminate model. In *Proceedings of the 19th International Conference on Soil Mechanics and Geotechnical Engineering*, Seoul, South Korea.

Maples, R. (2000). *Petroleum Refinery Process Economics*. PennWell Corporation.

Ng, C. (2008). Deformation and failure mechanisms of loose and dense fill slopes with and without soil nails. In *Proceedings of the 10th International Symposium on Landslides and Engineered Slopes*, pages 159–177, Xian, China. CRC Press.

Ng, C. (2009). What is static liquefaction failure of loose fill slope. In *The 1st Italian Workshop on Landslides*, volume 1, pages 91–102, Napoli, Italy.

Noriega, S. P. (2015). Characterisation of saturated loose sand samples prepared by fluidization.

Okamura, M. and Inoue, T. (2012). Preparation of fully saturated models for liquefaction study. *International Journal of Physical Modelling in Geotechnics*, 12(1):39–46.

Olson, S. and Stark, T. (2001). Yield strength ratio and liquefaction analysis of slopes and embankments. *Journal of Geotechnical and Geoenvironmental Engineering*, 129(8):727–737.

O'Rourke, T. and Lane, P. (1989). Liquefaction hazards and their effects on buried pipelines. Technical report, National Center for Earthquake Engineering Research.

Park, S.-S. and Byrne, P. (2004). Stress densification and its evaluation. *Canadian Geotechnical Journal*, 41:181–186.

Phillips, R. and Byrne, P. (1995). Modeling flowslides caused by static loading. *Transportation Research Record*, 1504:12–21.

Poulos, S., Castro, G., and France, J. (1985). Liquefaction evaluation procedure. *Journal of Geotechnical Engineering*, 111(6):772–792.

Puppala, A. J., Acar, Y. B., and Tumay, M. T. (1995). Cone penetration in very weakly cemented sand. *Journal of Geotechnical Engineering*, 121(8):589–600.

Rijkswaterstaat (1994). Design plan oosterschelde storm-surge barrier, overall design and design philosophy. Technical report, Ministry of Transport, Public Works and Water Management.

Roshan, A., Khalilpasha, H., and Ghorbani, M. (2010). Interaction of soil static and dynamic stiffness and buried pipeline under harmonic vibration. *American Journal of Engineering and Applied Sciences*, 3(2):441–448.

Sadrekarimi, A. (2014). Static liquefaction-triggering analysis considering soil dilatancy. *Soils and Foundations*, 54(5):955–966.

Silvis, F. and de Groot, M. (1995). Flow slides in the netherlands: experience and engineering practice. *Canadian Geotechnical Journal*, 32(6):1086–1092.

Skopek, P., Morgenstern, N., Robertson, P., and Sego, D. (1994). Collapse of dry sand. *Canadian Geotechnical Journal*, 31(6):1008–1014.

Stoutjesdijk, T., de Groot, M., and Lindenberg, J. (1998). Flow slide prediction method: influence of slope geometry. *Canadian Geotechnical Journal*, 35(1):43–54.

Takahashi, H., Kitazume, M., Ishibashi, S., and Yamawaki, S. (2006). Evaluating the saturation of model ground by p-wave velocity and modelling of models for a liquefaction study. *International Journal of Physical Modelling in Geotechnics*, 6(1):13–25.

Take, W. and Beddoe, A. (2014). Base liquefaction: a mechanism for shear-induced failure of loose granular slopes. *Canadian Geotechnical Journal*, 51(5):496–507.

Take, W., Bolton, M., Wong, P., and Yeung, F. (2004). Evaluation of landslide triggering mechanisms in model fill slopes. *Landslides*, 1(3):173–184.

Taylor, R. (1995). *Geotechnical Centrifuge Technology.* Blackie Academic & Professional.

Terzaghi, K. (1925). *Erdbaumechanik auf bodenphysikalischer grundlage.* F. Deuticke.

Terzaghi, K. (1943). *Theoretical soil mechanics.* John Wiley and Sons, New York.

Teymur, B. and Madabhushi, S. (2006). Centrifugal modelling of the landslides triggering mechanism in layered fill slopes. In *Physical modelling in geotechnics: 6th ICPMG '06*, pages 747–752. Taylor & Francis.

Tsukamoto, Y., Ishihara, K., Nakazawa, H., Kamada, K., and Huang, Y. (2002). Resistance of partly saturated sand to liquefaction with reference to longitudinal and shear wave velocities. *Soils and Foundations*, 42(6):93–104.

Ueno, K. (1998). Methods for preparation of sand samples. In *Proceedings of the International Conference Centrifuge 98*, volume 2, pages 1047–1055, Tokyo, Japan.

Vinegar, H., Waal, J. D., and Wellington, S. (1991). Ct studies of brittle failure in castlegate sandstone. *International Journal of Rock Mechanics and Mining Sciences & Geomechanics Abstracts*, 28(5):441 – 450.

Wanatowski, D. and Chu, J. (2012). Factors affecting pre-failure instability of sand under plane-strain conditions. *Gotechnique*, 62(2):121–135.

White, D., Take, W., and Bolton, M. (2003). Soil deformation measurement using particle image velocimetry (piv) and photogrammetry. *Geotechnique*, 53(7):619–631.

Whitman, R. (1985). On liquefaction. In *Proceedings of the 11th International Conference on Soil Mechanics and Foundation Engineering*, volume 4, pages 1923–1926, Rotterdam, the Netherlands. A.A. Balkema.

Yamamuro, J. and Lade, P. (1997). Static liquefaction of very loose sands. *Canadian Geotechnical Journal*, 35(6):905–917.

Yamamuro, J. and Wood, F. (2004). Effect of depositional method on the undrained behavior and microstructure of sand with silt. *Soil Dynamics and Earthquake Engineering*, 24:751–760.

Yamamuro, J., Wood, F., and Lade, P. (2008). Effect of depositional method on the microstructure of silty sand. *Canadian Geotechnical Journal*, 45(11):1538–1555.

Yoshimi, Y., Tanaka, K., and Tokimatsu, K. (1989). Liquefaction resistance of partially saturated sand. *Soils and foundations*, 29(3):157–162.

Zhou, S., Liu, L., Wang, B., Yang, L., and Gong, Q. (2002). Centrifugal model test on the stability of underwater slope. In Phillips, R., Guo, P., and Popescu, R., editors, *Physical modelling in geotechnics: ICPMG '02*, pages 759–764. Swets & Zeitlinger Lisse, A.A. Balkema.

A Calculation of slope angle

The rotation point and the ends of the potentiometer form a triangle (Figure 21). By measuring the three lengths of this triangle, the angle can be calculated by the cosine rule which is defined as

$$a^2 = b^2 + c^2 - 2bc\cos\alpha \tag{1}$$

Rearranging this equation gives

$$\alpha = \arccos\frac{b^2 + c^2 - a^2}{2bc} \tag{2}$$

When the platform is tilted, the change in length a is recorded by the *MP3* program. The length of side b does not change during tilting as it corresponds to the radius of the rotating circle. Since length c remains the same, the change in the angle α can be calculated by the values of the potentiometer. As the platform starts in horizontal position, the platform angle corresponds to the change in the calculated angle α. This was verified and confirmed by using an inclinometer to measure the angle directly. The position of the Microswitches was slightly changed throughout the test series; therefore the final slope angle varied between 20°and 22°.

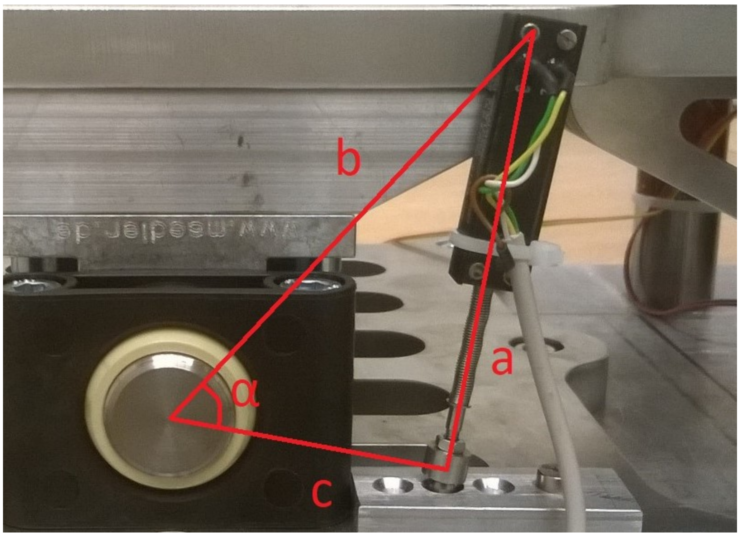

Figure 21: Calculation of the angle by the lengths of the triangle

B Modifications experimental set-up

As this project concerned a new design and preliminary series of experiments, modifications have been made in the set-up and procedure throughout the duration of the project. The most important adjustments are addressed below.

- When testing the fluidisation system, no proper upward flow was observed close to the inflow boundary due to a lack of holes in the thicker tube.

It was decided to place a PVC block to fill up this space to improve the uniformity of the fluidisation process.

- During the first preliminary experiments, four pressure sensors were attached to a rod which was loosely located on the bottom of the strongbox. In the following series of tests with water, three sensors were fixed on the filter with aluminium strips and screws.
- The upper granular filter was not completely flat and could be compressed. As it was assumed that this could lead to overestimation of the settlement measurement, a new filter was fabricated for the experiments with viscous fluid. Additionally, five holes were made in the filter to keep it flat with two bolts and to attach the PPTs on rods at the bottom.
- The PPTs appeared to become less accurate over time; they were replaced together with the new filter before the tests with viscous fluid.
- The added block inside the strongbox and the edges from the upperbox caused problems as sand remained on top and fell behind the block. Silicon was used to fix these edges and another block was put on top for the experiments with viscous fluid.
- Measurement tapes were placed inside the strongbox to read the layer height. They had to be replaced several times because they got damaged by sand and water.

C Preparation of viscous fluid

An aqueous solution of water and glycerol (glycerine) was initially used as viscous fluid for the centrifuge experiments. Due to the high solubility of glycerol, the viscous fluid was simply prepared by adding glycerol to water while stirring manually. The viscosity blending index (VBI) defined by Maples (2000) was used to calculate the mass percentages of water and glycerol to obtain the intended viscosity. Once the solution was prepared, the viscosity was determined by a *Model 35 Viscometer*, which measures the shear stress induced by a given shear rate. The viscosity can subsequently be calculated due to the linearity of Newtonian fluids. The kinematic viscosity expressed in centistokes (cSt) was obtained by dividing the dynamic viscosity by the fluid density, which was similar to the density of water. When the required viscosity was obtained, the mixture was put under vacuum for at least 12 hours to remove visible air bubbles.

As the amount of glycerol was limited, hydroxypropyl methylcellulose (HPCM) powder was added to obtain higher viscosities. The powder was added to hot water in a blender with continuous mixing; a blending time of at least 24 hours was required to obtain a homogeneous solution. This small amount of substance with high viscosity was then mixed in the container with the existing viscous fluid. The intended viscosity was obtained by measuring the viscosity in the viscometer and adding water or viscous substance. As the HPCM mixture was a non-Newtonian fluid, the dial readings of the viscometer were non-linear and the viscosity could not be accurately determined. Furthermore, a temperature difference up to 5°C between preparation and the experiments led to a discrepancy in measured viscosity of repeated tests, while the same fluid was used.

Adamidis and Madabhushi (2014) found an exponential increase in uncertainty with higher viscosities; while a viscosity of 10 cSt at 25°C decreases to 8 cSt with a temperature drop of 5°C, a viscosity of 50 cSt would change to 40 cSt. A higher uncertainty at higher viscosities was indeed observed.

D Fluidisation as sample preparation technique

Discharge

The appropriate vertical specific discharge for the fluidisation system of the large liquefaction tank was calculated to be 1E-3 m/s (de Jager, 2018). With an area of 10 m^2, a resulting volumetric flow of 10 l/s was applied to prepare the sample. As the material is the same and the fluidisation system for the centrifuge model was designed following the same principles, the suitable volumetric flow in the strongbox can be back calculated from its area:

$$Q = q * A = 1E - 3m/s * 0.048m^2 * 60 * 1000 = 2.89l/min \qquad (3)$$

where q is the specific discharge and A is the inner area of the strongbox. This means that a volumetric flux of approximately 3 l/min is sufficient to assess a fluidised sand bed in the strongbox.

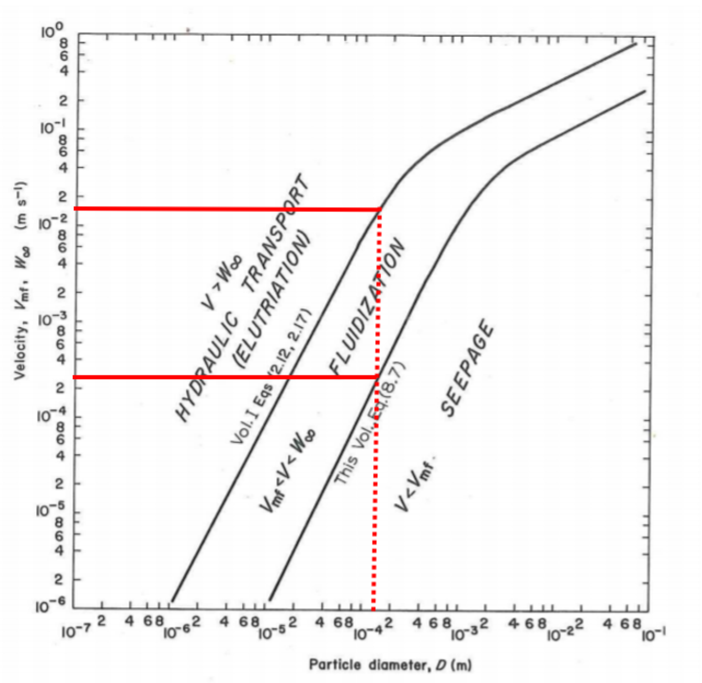

Figure 22: The critical fluidisation velocity of quartz spheres in water (Allen, 1984)

According to Allen (1984), a similar fluidisation process which he calls stationary fluidisation — as there is only vertical movement of the grains — can occur in natural sedimentary deposits. Since the geometry and flow conditions are comparable to the fluidisation system, the presented minimum fluidisation velocity can be compared. The obtained critical velocity is based on the pressure drop which reaches a constant value when the sand layer does not expand any longer. Equalizing the immersed bed weight to the pressure drop combined with the Carman-Kozeny equation, a range of fluidisation velocities in function of particle diameter is obtained (Figure 22). As the Geba sand used for the experiments has a D_{50} of 0.125 mm, the critical velocity is bounded by approximately 2E-4 and 2E-2 m/s, as indicated by the red lines. The earlier proposed flux of 1E-3 m/s needed to initiate fluidisation is found in this range.

Set-up

The experimental set-up for fluidisation of the sample consists of a centrifugal rotary pump which is connected by tubes to a container with supply fluid and on the other end to the valves of the strongbox. A valve is placed between the pump and strongbox to control the inflow, and a liquid flow metre (type *RS Pro Liquid Acetal Copolymer*) is added to measure the flux. In order to avoid overflow during fluidisation, a tube connected to the tab creating vacuum was used for the experiments with water to provide drainage from the top of the strongbox. When using viscous fluid a magnetic pump and additional tubes were used for drainage and to collect the fluid from outflow in another container. Figure 23 illustrates the fluidisation set-up in the centrifuge showing the flow metre, valve, containers and rotary pump.

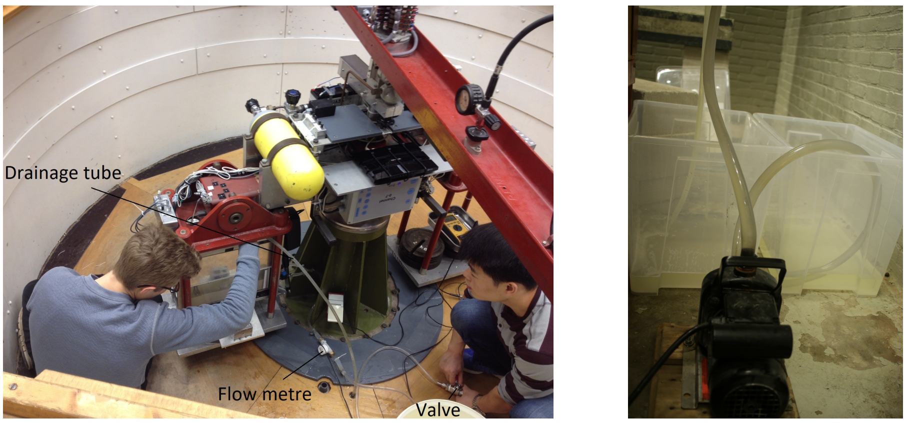

Figure 23: Experimental set-up for fluidisation in centrifuge

In ideal case a loop is created between inflow and outflow so the fluidisation supply is unlimited. However, as sand flows out during drainage, the outflow fluid is collected in another container to weight the mass and to protect the fluidisation system. Applying a filter on the tubes did not work as the small grain particles clogged the filter and the inflow flux decreased rapidly. At a viscosity of 50 cSt the magnetic pump was dysfunctional; a thick tube was used to lower the water table in the strongbox by using hydraulic head difference.

When opening the valve completely, the flow metre indicated a discharge of approximately 5 l/min when using water. It was observed that this maximum flux was necessary to fluidise the sand layer completely. It was therefore decided to open the valve entirely during each fluidisation procedure. After a couple of preliminary tests, the flow metre was taken out of the chain due to practical reasons. The discharge with viscous fluid was not measured; by considering the duration of the supply fluid, it was clear that the discharge decreased with increasing viscosity. However, the measured pressures showed similar values and the obtained height of the fluidised sample was not affected.

Procedure

Each fluidisation procedure was preceded by starting the MP3 software to record the measurement of PPTs. When all tubes were connected and the two valves on the strongbox were opened, the pump was started and the valve to control the inflow was opened up completely. As the sand was stiff after each centrifuge experiment, manual stirring was used to loosen the sample and obtain uniform fluidisation of the sample. When the sand appeared to be homogeneous, fluidisation was continued without stirring until the fluid supply was insufficient. Meanwhile the magnetic pump was used to drain the water from the top to prevent overflow. The total fluidisation time varied between 1.5 and 5 minutes and the procedure was repeated when the surface was not sufficiently flat. When the inflow was closed, the sand started to settle uniformly while the excess pore pressures dissipated. The water level was lowered to a level of approximately 18 cm. The layer height was determined from the measuring tapes. After each experiment with viscous fluid, the liquid was transferred to the supply container by a tube and filter using hydraulic head difference. The remaining sand was collected, put in the oven to dry and weighted after at least 24 hours.

Although it was difficult to exactly repeat the protocol when preparing the sample, the total fluidisation duration was of less importance as long as the expanded sand bed reached its maximum height. Albeit small variations in density and flatness were observed, the reproducibility of the initial samples by this preparation technique was considered acceptable.

Observations

Apart from laboratory investigation of the fluidised sample properties, observations of interesting phenomena during fluidisation were made. Four photographs of the fluidisation process with a viscous fluid of 4 cSt are shown in Figure 24. Note that only a fraction of the sample is visible due to limitations of the camera position. Two important phenomena which were observed during each fluidisation cycle are visible:

- When a centrifuge experiment including failure is finished, a new sample is prepared by fluidisation for the next test. When opening the valve to fluidise the sand, a horizontal gully is formed around two centimetres above the bottom, and the fluid flows in horizontal direction towards the boundary where it goes up. Stirring is necessary to make sure the sample becomes loose and water flows up uniformly. This phenomenon implies that the horizontal permeability is higher than in vertical direction, and that resistance to flow is probably lowest at the shorter side walls.

- Some columns of fluid flowing upwards are formed as the fluid follows the path of least resistance. However, it seems that this only happens at the walls and not in the middle of the sand layer. One possible explanation is that the fluid escapes through the screw holes along the boundary rather than flowing through the filter.

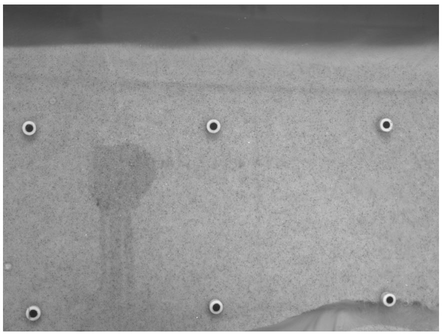

(a) Frame 1: right after opening valve

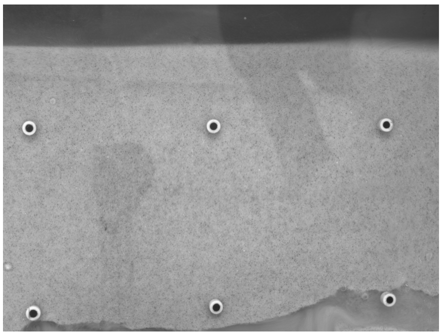

(b) Frame 2: a horizontal gully is formed

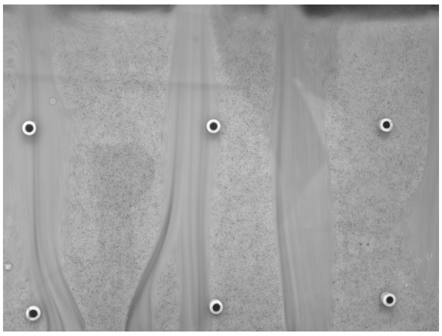

(c) Frame 3: after stirring, columns are formed

(d) Frame 4: before closing valve, more uniform upward flow

Figure 24: Four chronological frames during fluidisation

When the valve is closed, the settlement of the sand layer develops uniformly. Figure 25 shows six chronological frames during resedimentation of the sand which results in a flat sand bed. As the grains can be separated due to the high resolution, it is clear that settlement occurs in horizontal layers which settle uniformly one by one. The black line indicates the height of the layer which has come to rest while the grains above are still falling down. No additional movement in the grains below this line is observed in the following frames.

Note that only the upper half of the sample is visible. It is unclear whether the same process can be observed closer to the bottom. The lower part is believed to be not properly subjected to fluidisation due to the high self weight, limitation of upward flow and presence of sensors, and that the fluid might flow upwards through looser column paths with low resistance. It is therefore assumed that the uniformity is higher in the upper part of the layer, as the sand mass is flowing and settling simultaneously.

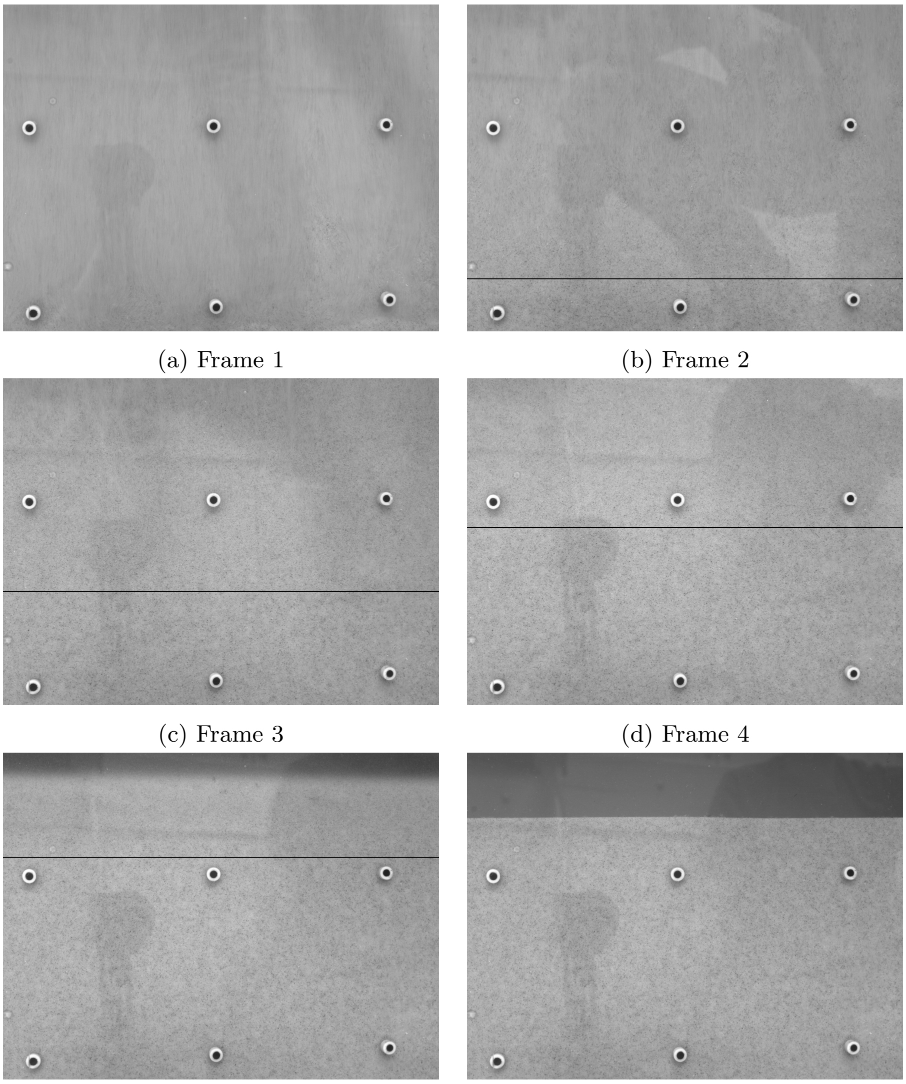

(a) Frame 1 (b) Frame 2

(c) Frame 3 (d) Frame 4

(e) Frame 5 (f) Frame 6

Figure 25: Six chronological frames during settlement after fluidisation

E Calculation of relative density

The calculated average density for all experiments is expressed as relative density, which is defined as:

$$D_r = \frac{e_{max} - e}{e_{max} - e_{min}} \tag{4}$$

with

$$e = \frac{n}{1-n} = \frac{V_s - V_t}{V_s} = \frac{m_s/\rho_s - V_t}{m_s/\rho_s} \tag{5}$$

where e_{min} and e_{max} are the minimum and maximum void ratio, respectively, e is the void ratio, n the porosity, V_s the volume of the sand, V_t the total volume, m_s the mass of the sand and ρ_s the density of the sand.

The values for minimum (0.64) and maximum (1.07) void ratio and the specific density (2.67 g/cm^3) are adopted from previous research (see Section 3.6). The total volume is calculated by multiplying the area (length x width) with the average height of the sand layer and subtracting the volume of cables and sensors in the sample. The average height is determined from the measuring tapes on the plexiglass; the volume of the sensors is measured by submerging them in a cylinder and the volume of the cables is calculated by the diameter and length. The volume of the sand is attained by the mass and density of the sand.

Unfortunately, the design of the strongbox and the fluidisation procedure complicated the measurement of the sand mass. It was visibly clear that a considerable and varying amount of sand was left behind on top of the PVC block and edges of the upperbox (Figure 26). Furthermore, the initial measurement of dry sand did not match the mass of sand which was weighted at the end of the experiments; although the flushed sand was collected and weighted, measurements showed that more sand was lost during each test. The total amount of missing sand was therefore divided over the number of experiments and this value was added to the used value of sand mass for each test. The inaccuracy of measuring the sand mass might have led to overestimation of the average relative density.

Figure 26: Sand left on the upperbox edges and PVC block

F Investigation degree of saturation

Samples from the strongbox after fluidisation of the sand were taken to measure the degree of saturation by the mass-volume method. A cylindrical cup of 100 ml with known mass and a tube were filled with de-aired water. Difference in hydraulic head was used to transport the submerged sand from the strongbox into the cup. When a sand level of approximately 65 cm was reached, the water table was lowered close to the surface. The cup was placed on a vibration table for a few seconds in order to make the surface flat. The water table was held slightly above the sand surface to make sure the sand remained submerged. The volume corresponding to the sand and water height were measured, together with the mass of the total sample. The sand was flushed into a bowl and put to dry in the oven for at least 24 hours. Afterwards the dry mass of the sand was measured. The mass of the water was back calculated by subtracting the mass of the cup and sand from the total mass. As the densities of water and sand were known, the degree of saturation could subsequently be calculated by the volume of water and voids:

$$S_r = \frac{V_w}{V_v} = \frac{V_w}{V_t - V_s} \tag{6}$$

where V_w is the volume of water (calculated from the mass and density of water), V_v is the volume of voids, V_t is the total volume (measured) and V_s is the volume of sand (calculated from the mass and density of sand).

The propagation of error is used to quantify the accuracy of the results. The calculated values of the four samples are listed in Table 7. To quantify this method, two additional tests were performed where the cup was filled with de-aired water only, giving a Sr of 99.5 and 99.8%.

Table 7: Calculation of S_r

	Sample 1	Uncertainty	Sample 2	Uncertainty	Sample 3	Uncertainty	Sample 4	Uncertainty
Measured properties								
Volume sand level (ml)	62	1	64	1	64	1	65	1
Volume water level (ml)	67.0	0.5	70.5	0.5	69.8	0.5	69.5	0.5
Mass cup (g)	116.4	0.1	116.4	0.1	116.4	0.1	116.4	0.1
Mass total (g)	239.4	0.1	245.5	0.1	240.8	0.1	242.2	0.1
Mass sand (g)	89.8	0.1	94.6	0.1	88.3	0.1	90.6	0.1
Assumed properties								
Density water (g/cm^3)	0.998	0.002	0.998	0.002	0.998	0.002	0.998	0.002
Density sand (g/cm^3)	2.67	0.02	2.67	0.02	2.67	0.02	2.67	0.02
Calculated properties								
Mass water (g)	33.3	0.2	34.6	0.2	36.1	0.2	35.2	0.2
Volume water (cm^3)	33.4	0.2	34.6	0.2	36.2	0.2	35.3	0.2
Volume sand (cm^3)	33.6	0.3	35.4	0.3	33.1	0.3	33.9	0.3
Volume total (cm^3)	67	1	71	1	70	1	70	1
Volume voids (cm^3)	33.4	0.6	35.1	0.6	36.7	0.6	35.6	0.6
Degree of saturation (-)	1.0	0.0	1.0	0.0	1.0	0.0	1.0	0.0
Degree of saturation (%)	99.9	1.8	98.7	1.7	98.7	1.6	99.2	1.7

G Investigation uniformity by CT-scanner

The results from the CT-scanner show the object in slices of 0.6 mm with pixels corresponding to CT numbers. This gray scale or so called Hounsfield scale is a qualitative description for the radiodensity. It is linearly calibrated by the attenuation coefficients of water and air. Pure water is defined as zero Hounsfield Units (HU) while air has a value of -1000 HU. Assuming a fully saturated porous medium of two phases which are grain material and water, the Hounsfield scale can be linearly related to the bulk density and porosity.

Two plastic cylindrical cups (Figure 27) were initially prepared with a dense and loose sample. The porosity was calculated by measuring the mass and volume of the sand. After scanning the samples, the radiodensity in Hounsfield units was linearly correlated to the known porosity. However, after a first scan to check the feasibility of scanning the strongbox, it was clear that the order of magnitude in radiodensity was incomparable due to the difference in material. The reflections of either plastic or metal as surroundings make a big difference in the radiodensity of the saturated sand.

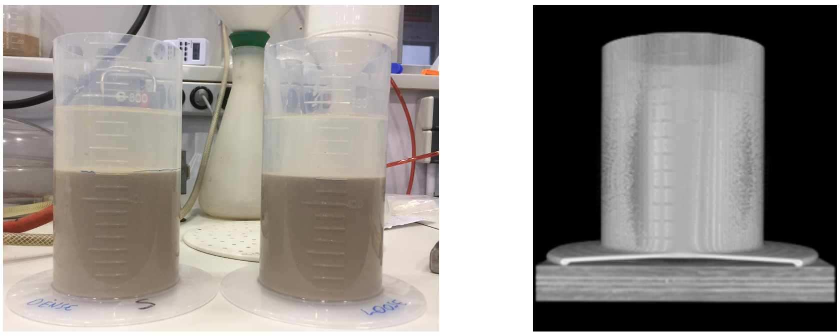

Figure 27: Two prepared samples (left) and corresponding 3D view from the CT-scanner in Hounsfield scale (right)

In order to relate the HU to the relative density of the sand in the strongbox, the porosity was calculated by using the measured volume (by the height of the measuring tapes). This value was related to the average value of HU over the sample; it was found that the pure quartz material corresponded to a value of approximately 1660 HU; this value was used as correlation factor to assess the porosity. The measured values in gray scale of several cross sections of the strongbox could then be scaled to calculate the porosity or relative density. The correlation factor was used for another scan of the strongbox and it showed that the calculated porosity was equal to the measured porosity from the volume. As the metallic material (filter, PPTs, walls) caused significant noise, there exists uncertainty in the absolute values of porosity. However, by comparing similar sections of different scans of the strongbox, the variation in porosity could be analysed. Consequently, the relative density corresponding to the porosity was calculated and used for consistency.

The first scan was made from a sample which was subjected to a gravity acceleration of 70g; the main purpose of this scan was to check the feasibility of scanning the strongbox. Afterwards another four scans were performed to eval-

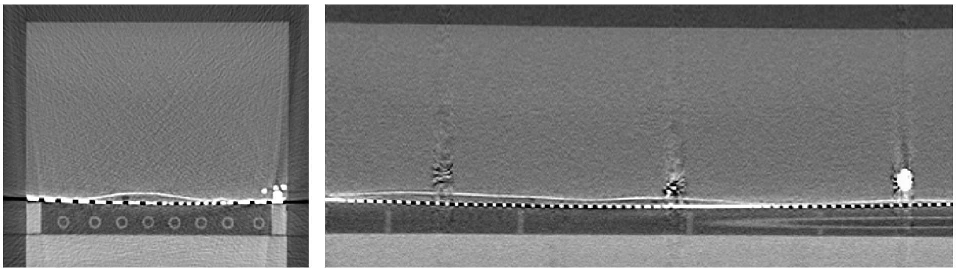

(a) Width (b) Length

Figure 28: Lateral and longitudinal cross section of the scanned strongbox

uate the density after fluidisation. Figure 28 shows the the cross sections over the width and length of the strongbox. Scanning the entire strongbox required moving the table, which caused a shock and disturbance of the sample. To overcome this problem the largest possible *slice* (having a thickness of 3 cm) without moving the table was scanned before and after fluidisation. Afterwards the table was moved again to observe the difference in density caused by the impact. Table 8 gives an overview of all performed CT-scans for this project. The cross section of the undisturbed slice is used to quantify the variation in density over the height and width after fluidisation, while the scan of the total strongbox is used to evaluate the density profile over the length in both the liquefied upper and undisturbed lower part. Figure 29 shows a 3D view of the analysed volume of both the total strongbox and the slice.

Table 8: Overview of CT scans

Name	**Description**
CT1	Loose sample in plastic cylinder
CT2	Dense sample in plastic cylinder
CT3	Full scan of strongbox after centrifugal acceleration at 70g
CT4	Full scan of strongbox after fluidisation, but disturbed by movement of the CT-table
CT5	Same sample as CT4 but only a slice (disturbed)
CT6	Scan of slice after fluidisation (undisturbed)
CT7	Scan of slice after intentionally moving the table

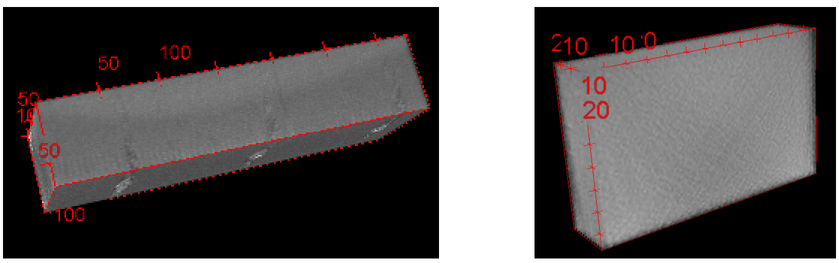

Figure 29: Analysed volume of total strongbox (left) and slice (right)

Comparing the cross sections of the slice before and after moving the table shows how the density variation changed due to the shock and assumed liquefaction of the top layer. Figure 30 illustrates that the relative density variation over the width increased with 20–30%. The difference in the middle is slightly higher than at the boundaries; this is a consequence of the initial density variation, which shows a curvature in profile with lower density in the middle. Hence, the thickness of the liquefied sand layer is higher in the middle.

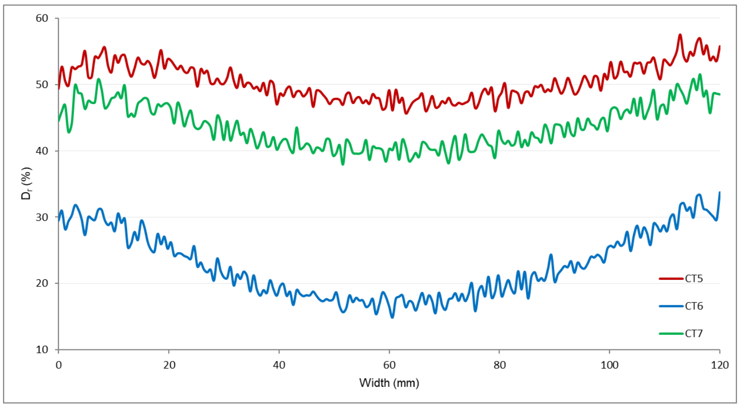

Figure 30: Change in relative density along the width

Figure 31 shows the change in relative density along the depth, which varies between an increase of 30–60% at the top towards 5% around the transition area. The denser bottom layer, which is assumed to be only affected by the initial shear deformation and not subjected to liquefaction, shows an increase in density of maximum 5%. When considering the average relative density of the sample (dashed lines), it is clear that after disturbance the relative density at the bottom and top will be highly over- and underestimated, respectively.

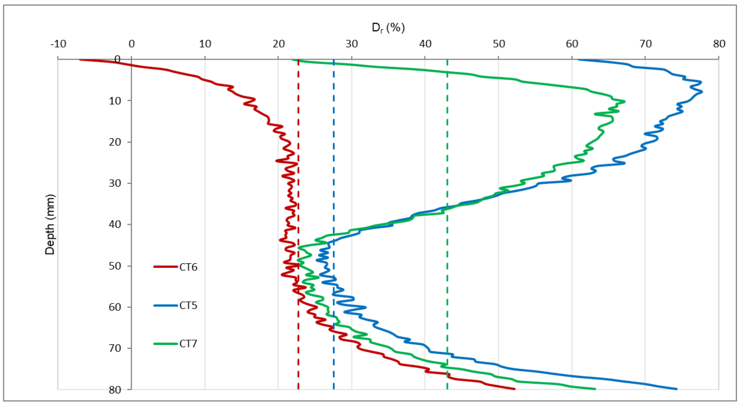

Figure 31: Change in relative density along the depth

The density profile over the length can be analysed by scan CT4, though the disturbance should be taken into account. As illustrated in Figure 32, nine selections of equal area were selected over the height of the sample. The average density of each selection along the length of the sample was determined to evaluate the density profile. It shows that the top layer suffered a rise in relative density of approximately 30% due to liquefaction. Despite the artefacts caused by reflections of the cables and sensors, the lower layer yields a uniform profile. Analysing the section in the middle clearly indicates the curvature of transition between the denser upper and looser bottom part. Similar to the lateral density profile (Figure 30), the disturbance reaches a larger depth in the middle compared to the boundaries.

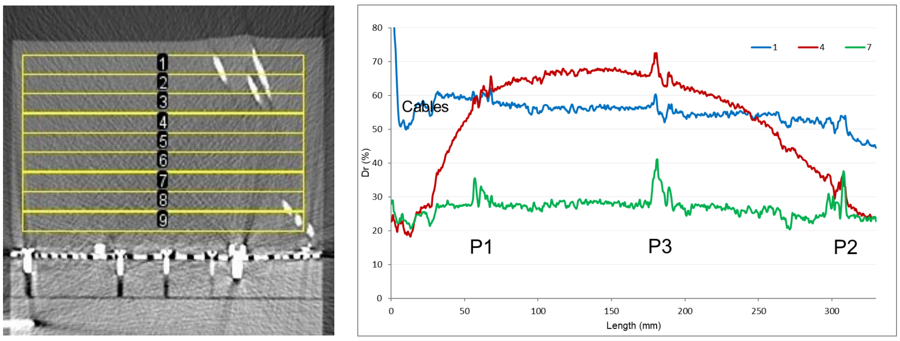

Figure 32: Change in relative density along the length

H Overview tilting experiments

A detailed overview of the tilting experiments in the centrifuge with the important parameters is presented in Table 9, where $D_{r,0}$ and H_0 are the initial relative density and layer height, respectively, and $D_{r,Ng}$ and H_{Ng} are the relative density and layer height before tilting at the intentional gravity level. The last column indicates the time between fluidisation and the start of the centrifuge. This overview is limited to the relevant experiments which were used for the analysis of the results in this report. Note that the test numbers are not chronological as other performed tests are excluded. It should be furthermore mentioned that experiments W07 and W21 with water as pore fluid were preliminary tests with a slightly different set-up, as outlined in Appendix B.

Table 9: Overview of tilting experiments

	Fluid viscosity				Average relative density		Average height		
Test name	Intended	Measured	g-level	Tilting rate	$D_{r,0}$	$D_{r,Ng}$	H_0	H_{Ng}	Failure angle
	cSt	cSt	N	°/s	%	%	cm	cm	°
W07	-	1	1	0.1	39	-	7.3	-	17.2
W21	-	1	1	0.1	29	-	9.1	-	16.8
V01	-	5	1	0.1	29	-	9.0	-	11.0
V02	-	4	1	0.1	33	-	8.7	-	13.3
V03	3.2	3	10	0.1	26	47	8.7	8.3	-
V04	3.2	3	10	2.0	27	38	8.7	8.4	9.9
V05	3.2	3	10	1.0	31	41	8.5	8.3	11.5
V06	3.2	3	10	0.5	27	35	8.5	8.4	12.5
V07	3.2	3	10	0.1	23	34	8.5	8.3	17.7
V08	10	9	10	0.1	23	35	8.4	8.2	14.3
V09	10	8	10	0.1	28	40	8.1	7.9	16.2
V10	5.5	6	30	2.0	26	42	9.4	9.1	9.1
V11	5.5	6	30	0.1	28	45	9.3	9.0	17.2
V12	5.5	6	30	0.1	29	46	9.2	8.9	18.5
V15	7.1	7	50	0.1	31	52	9.0	8.6	-
V16	7.1	7	50	0.1	28	49	9.0	8.6	16.3
V17	7.1	7	50	0.1	28	49	8.9	8.5	-
V18	30	30	30	0.1	25	45	8.9	8.5	10.5
V19	30	30	30	0.1	33	49	8.7	8.4	10.8
V20	50	50	50	0.1	29	53	8.7	8.3	13.0
V21	50	50	50	0.1	33	54	8.7	8.3	10.1

	PPT peak at start centrifuge				PPT peak at failure				
Test name	$P1_{start}$	$P2_{start}$	$P3_{start}$	$r_{u,start}$	$P1_f$	$P2_f$	$P3_f$	Fluidisation time	End fluidisation - start centrifuge
	kPa	kPa	kPa		kPa	kPa	kPa	s	s
W07	-	-	-	-	-	-	-	-	-
W21	-	-	-	-	0.44	0.12	0.06	180	-
V01	-	-	-	-	0.26	0.25	0.31	151	-
V02	-	-	-	-	0.46	0.27	0.32	300	-
V03	0.22	0.22	0.23	0.32	-	-	-	200	2335
V04	0.17	0.07	0.09	0.16	2.41	0.02	1.06	165	1511
V05	0.17	0.09	0.10	0.17	2.43	1.12	1.75	150	8220
V06	0.21	0.12	0.13	0.23	2.56	1.70	2.26	120	1269
V07	0.11	0.01	0.05	0.08	1.92	1.81	1.72	120	1875
V08	0.27	0.14	0.20	0.30	5.05	3.25	4.07	120	4237
V09	0.23	0.12	0.14	0.25	4.53	2.93	3.60	150	2154
V10	0.29	0.18	0.21	0.30	11.25	6.52	8.66	140	1488
V11	0.25	0.12	0.13	0.23	12.25	7.76	9.57	128	1320
V12	0.26	0.17	0.12	0.25	13.06	7.44	8.93	180	2108
V15	0.33	0.32	0.32	0.45	-	-	-	95	1377
V16	0.28	0.05	0.07	0.18	18.50	9.77	11.39	120	2700
V17	0.37	0.17	0.19	0.34	-	-	-	200	1382
V18	0.41	0.23	0.27	0.43	16.62	10.76	12.30	170	4096
V19	0.15	0.07	0.09	0.15	15.72	9.92	10.53	160	1436
V20	0.31	0.19	0.19	0.33	24.75	15.97	19.04	155	3047
V21	0.21	0.07	0.09	0.18	24.88	14.38	17.76	230	2772

I Consolidation theory

The relationship between failure angle and permeability can be explained by considering the fundamentals of soil mechanics. Instability will occur when the excess pore pressures induced by shear deformation cannot dissipate quickly enough, i.e. the transition from drained to undrained behaviour. The seepage time is limited by the consolidation rate, which depends on the permeability, layer thickness, compressibility and boundary conditions.

As the lower boundary and the side walls of the strongbox are closed, the problem can be simplified to a one dimensional consolidation problem. With similar loading rate, the dissipation or seepage rate can be defined following Terzaghi's theory as (Terzaghi, 1943)

$$\frac{\delta u}{\delta t} = c_v \frac{\delta^2 u}{\delta z^2} \tag{7}$$

where z is the drainage length and c_v is the consolidation coefficient defined as

$$c_v = \frac{k}{\gamma_w m_v} \tag{8}$$

with γ_w the unit weight of water, m_v the compressibility and k the hydraulic conductivity which can be written as

$$k = \frac{\kappa \rho g}{\mu} \tag{9}$$

in which κ is the intrinsic permeability, ρ is the fluid density and μ is the dynamic viscosity. Simplifying this partial differential equation shows that drainage is controlled by a dimensionless time factor defined as

$$T = \frac{c_v t}{L^2} \tag{10}$$

where t is time and L the length of the drainage path. With equal model height and consolidation coefficient, the time to dissipate excess pore pressures will be equal at any gravity level. This implies that the seepage rate in a model with the same drainage length is solely influenced by the consolidation coefficient:

$$\frac{\delta u}{\delta t} \sim \frac{\kappa}{\mu m_v} \tag{11}$$

The intrinsic permeability of the sand remains unchanged and has no influence. When the hydraulic conductivity is decreased by increasing the viscosity of the pore fluid, the seepage rate is lower and instability occurs at a lower angle. When plotting the failure angle versus a factor which includes the length and viscosity (corresponding to the consolidation rate), a trend of increasing failure angle with higher seepage rate is visible (Figure 33). It should be noted that some discrepancies in the test results are caused by disturbance of the samples.

A total of four preliminary experiments in the centrifuge model at 1g were performed with different viscosities and small variations in height. Comparing the consolidation rate with failure angle, the observed trend seems to have a logarithmic shape (Figure 34). As the initial density of the samples was not affected by the centrifuge start when tilting at 1g, is it interesting to compare the results with the tests in the large liquefaction tank (de Jager, 2018). Despite the significant difference in dimensions, the failure angle obtained in the large tank can be found in line with the extended logarithmic trend line from the results of the small centrifuge model. The shape of the trend line can be explained by considering the compressibility of soils, which decreases logarithmically for increasing mean effective stress and depth.

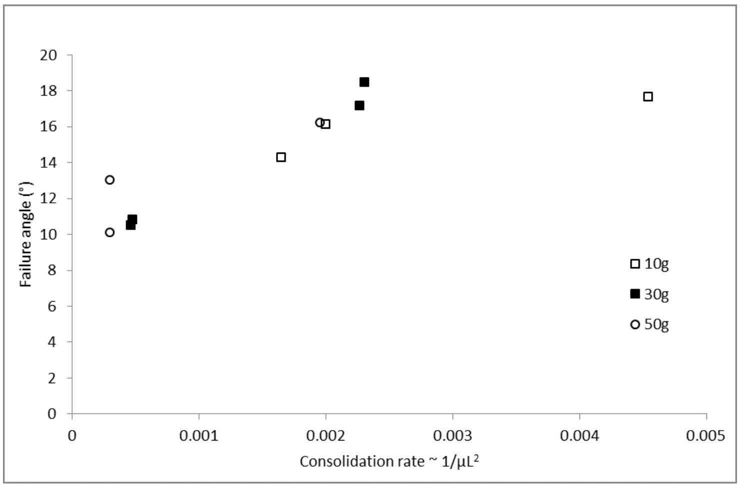

Figure 33: Relationship between consolidation rate and failure angle at various gravity levels

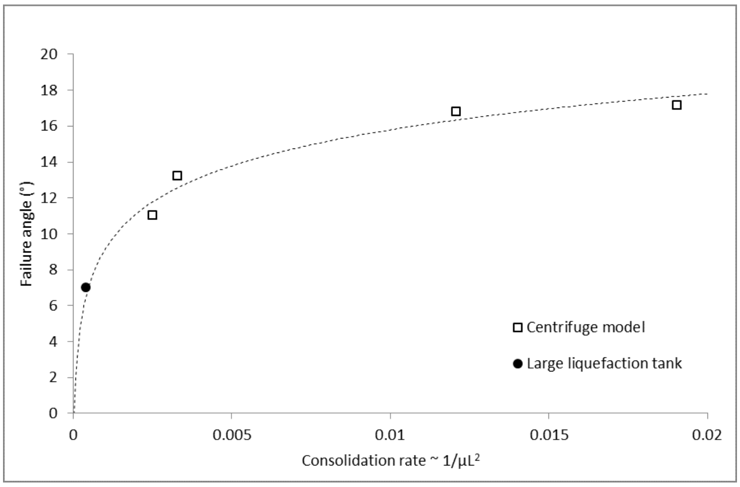

Figure 34: Relationship between consolidation rate and failure angle at 1g

J Disturbance due to acceleration rate

The acceleration rate of the centrifuge towards the required gravity level causes problems when pore fluids with high viscosities are used. The loading rate during consolidation is then exceeding the dissipation rate of the pore fluid leading to liquefaction and severe densification of the top layer. The centrifuge was initially accelerated to the required gravity level with a rate of approximately 1.3 RPM/s, but samples with water already liquefied during acceleration. Decreasing the rate to a minimum of 0.1 RPM/s solved this problem for most experiments. However, the seepage rate with a viscosity of 50 cSt was insufficient and the samples were disturbed during acceleration (Figure 35). It should be noted that the moment of disturbance occurs at the same g-level and corresponding pressures for both tests; this indicates a high reproducibility of the centrifuge experiments.

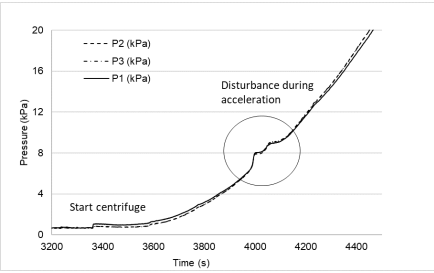

(a) Test V20

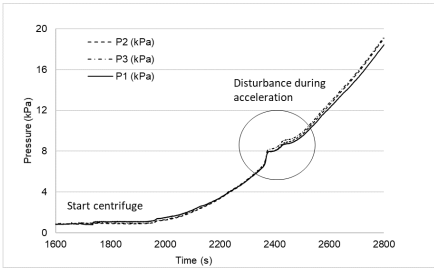

(b) Test V21

Figure 35: Pressure response during acceleration with a viscosity of 50 cSt

K Disturbance due to start centrifuge

One important mechanical problem which needs more attention is the start of the centrifuge. The sudden acceleration perpendicular to the long axis of the sample causes shear deformation, sudden excess pore pressures and subsequently liquefaction of the top layer. As the basket pivot forms an angle when the centrifuge is started, the flat sand bed forms a small inclination. Due to the start and following liquefaction, sand flows towards the centre of the centrifuge, opposite to the induced slope direction during tilting. The displacement is illustrated in Figure 36, where the green tint indicates the initial layer height and the purple tint defines the layer surface after the centrifuge start. This effect is not beneficial as it causes shearing of the sand layer in the opposite direction of the intended slope and densification of the top layer.

Although the direction of impact is along the width instead of the length, it is assumed that the effect is comparable to the disturbance caused by moving the table of the CT scanner (see Appendix G). This means a large increase of density at the top while the lower layer is hardly affected; using the average density is therefore not a suitable measure. The magnitude of disturbance can be quantified by the measured peak in pressures, which corresponds to the thickness of the liquefied layer. Consider the pore pressure ratio which is defined as

$$r_u = \frac{\Delta u}{\sigma_v'} \tag{12}$$

where Δu is the change in pore pressure and σ_v' is the initial effective stress.

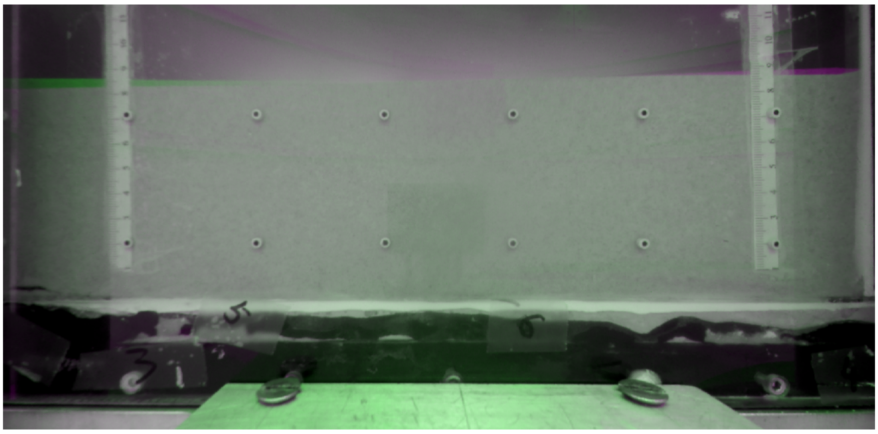

Figure 36: Sand layer before (green) and after (purple) centrifuge start

Using the average change in pressure of the three PPTs at the start of the centrifuge and an estimated effective unit weight of 8 kN/m^3, this ratio can be used to quantify the disturbance at the start of the centrifuge:

$$r_{u,start} = \frac{P1_{start} + P2_{start} + P3_{start}}{3 * 8 * H_0} \tag{13}$$

where H_0 is the initial height of the sand layer.

L Calculation errors due to gravity effects

Variation over depth

The effective radius can be calculated by subtracting the thickness of the basket and tilting frame plus two-thirds the model height from the total radius of the centrifuge. Considering a sand layer with a maximum height of 0.11 m gives

$$R_e = 1.22 - 0.025 - 0.155 - \frac{2}{3} * 0.11 = 0.967m \tag{14}$$

According to Taylor (1995), the maximum error caused by the variation of stress level with depth can be obtained by equating the maximum under- and over-stress:

$$r_u = r_0 = \frac{h_m}{6R_e} \tag{15}$$

where h_m is the model height and R_e is the effective radius. In our model the maximum error is thus

$$r_0 = \frac{0.11}{6 * 0.967} = 1.9\% \tag{16}$$

Although this error is minor during acceleration, it will increase when the strong-box is tilted at a certain gravity level. The variation in radius will create a rising stress difference between the crest and toe of the slope. Considering a maximum tilting angle of 20 degrees, the largest difference in radius can be calculated by the length of the sample as

$$\Delta r = L \sin 20° = 0.354 * \sin 20° = 0.121m \tag{17}$$

The maximum difference in radius between the two outer edges of the sample when it is fully tilted corresponding to the difference in g-level is then $\Delta r/R_e =$ 12.5%. The error in terms of stress difference can be calculated by Equation 16 and equals 2.1%. Adding this number to the initial error in over-stress gives a total maximum error of 4.0%.

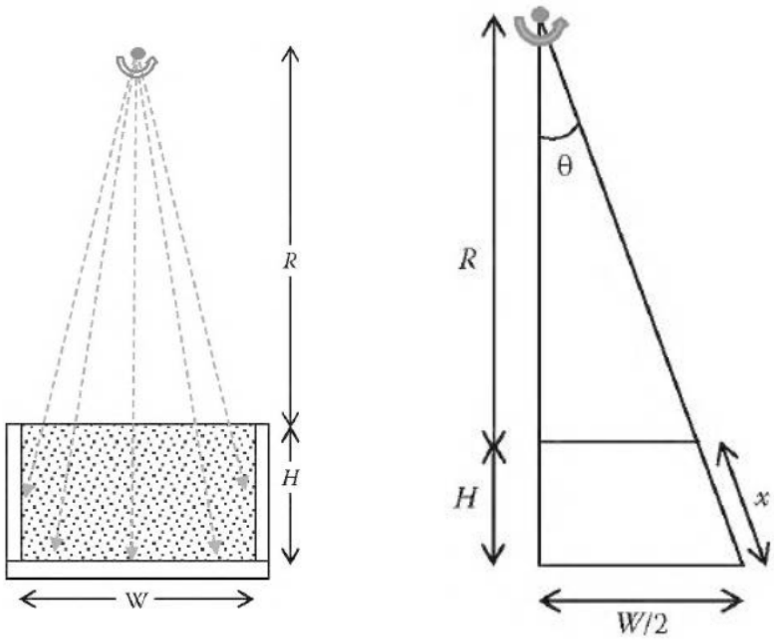

Figure 37: Radial gravity field and quantification of error (Madabhushi, 2015)

Variation over width

The radial distribution of gravity forming a curvature along the width of the sample is illustrated in Figure 37. According to Madabhushi (2015), the error can be obtained by the difference of radii at the centre and the edge of the sample:

$$\epsilon_{radial} = \frac{x - H}{H} * 100 \tag{18}$$

where H is the height of the sample and x can be calculated as function of the angle θ:

$$x = \frac{H}{\cos \theta} \tag{19}$$

and

$$\theta = \frac{W}{2(R+H)} \tag{20}$$

With a width (W) of 0.354 m, a layer height (H) of 0.11 m and a radius (R) which measures 0.931 m, filling in Equation 18 gives a radial error of 0.207%.

Coriolis effects

Due to the rotating acceleration field, particles might experience Coriolis effects during displacement in the plane of rotation (Figure 38). According to Taylor (1995), the Coriolis effect is assumed to be negligible if the ratio of Coriolis acceleration over inertial acceleration in the model is less than 10%. This implies that the velocity of a mass inside the model should be smaller than 0.05 times the radial velocity of the centrifuge model itself:

$$v < 0.05V \tag{21}$$

where v is the velocity of a mass within the model and V is the velocity of the model in centrifuge flight. At an angular velocity of 10 rad/s (corresponding to 10g), velocity V will be 9.67 m/s and the upper bound is then given by

$$v < 0.05V = 0.48m/s \tag{22}$$

The rate of displacement within the model during consolidation and tilting is unknown but certainly in the order of mm/s, so Coriolis effects can be considered negligible up to the moment of failure. The velocity of the moving sand mass during the flow slide should be investigated to verify if Coriolis effects need to be considered when analysing the post-failure behaviour; however, this falls outside of the scope of this report.

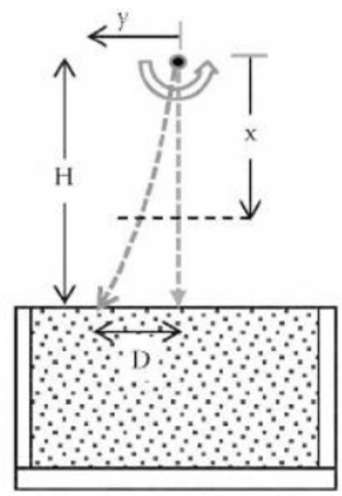

Figure 38: Illustration of the Coriolis effect on the model (Madabhushi, 2015)

M Settlement of the sand bed

The average relative density at each gravity level (defined as $D_{r,Ng}$ in the overview) is calculated by the change in height due to settlement. One frame from the video footage of the initial sample is compared to another frame just before tilting, when consolidation is finished (see Figure 39). The difference in layer height is measured by the software *ImageJ* by considering the average change in height of ten locations along the length. The obtained value is subtracted from the initial height and the result is used to calculate the relative density of the sample, as explained in Appendix E.

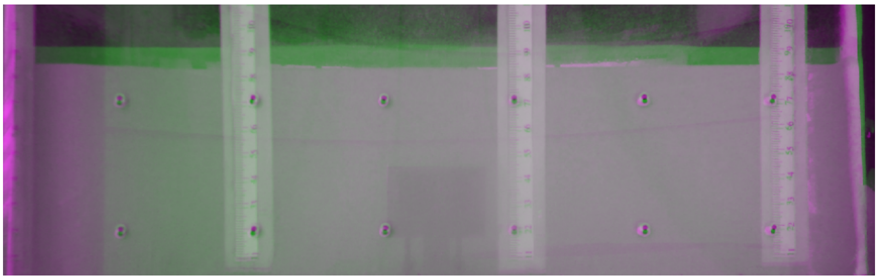

Figure 39: Change in layer height (green) due to gravitational acceleration

One experiment was performed to evaluate the settlement and corresponding density at various gravity levels. The sample was subjected to an acceleration of 10g up to 70g with steps of 10g. At each stage the settlement was measured as explained above. The consolidation curve was obtained by plotting the gravity factor N on a logarithmic scale versus the calculated void ratio (Figure 40). The lower value at 10g, which causes a small bump at 20g, is a result of the centrifuge disturbance at the start; initial liquefaction and densification leads to a higher measured settlement at 10g. The results of the tilting tests are added to show the variation in void ratio, a result of sample disturbance and inaccuracy of mass measurement. The graph also shows that the viscosity has no effect on the magnitude of compression or settlement.

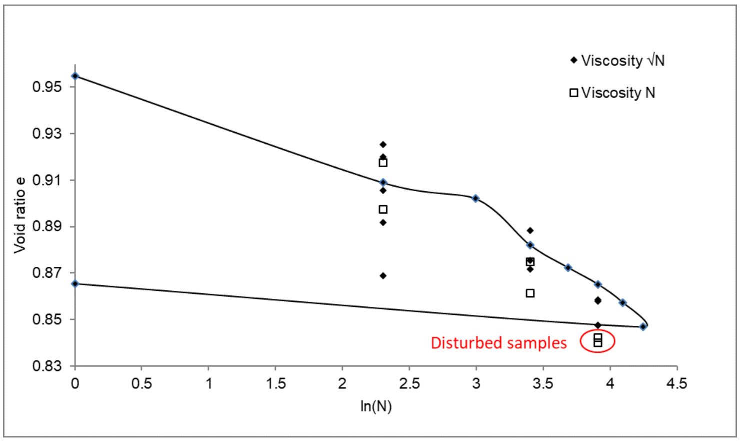

Figure 40: Diagram of void ratio versus gravity level

N Practical recommendations

The design of the sample box and the procedure of centrifuge experiments are both new; during the series of tests several modifications have been made to improve the quality of the experiments. There still exist several factors which can be improved, and other uncertainties should be quantified:

- The mechanical start of the centrifuge has to be improved to avoid any disturbance of the sample.
- The design of the strongbox should be modified for a more accurate measurement of sand mass and volume. Consequently, the error of the obtained average relative density will be smaller.
- The viscosity of the viscous fluid should be determined more accurately and the effect of shear-dependency should be investigated. Furthermore a constant temperature should be assured to avoid any fluctuation in viscosity measurements.
- The viscous fluid (both glycerine and HPMC solutions) should be used in an element test to investigate any influence on the soil properties. According to previous research (Askarinejad et al., 2014; Dewoolkar et al., 1999), there should be no significant effect.
- The data logging rate should be increased so the exact peak value of pore pressures during failure can be captured.

O Removing fish eye distortion and comparison of images

The software *MATLAB* was used to remove the fish eye effect from the recorded GoPro images. A set of 15 checkerboard calibration images with known square dimensions (Figure 41) was gathered and stored in the appropriate folder. The first part of the script was run to obtain the calibration parameters which were used to remove the lens distortion from the GoPro images. The second part of the script was executed to make a montage of two images in order to highlight the change in the surface of the sand layer due to a flow slide or settlement. The full MATLAB script is displayed in Figure 42.

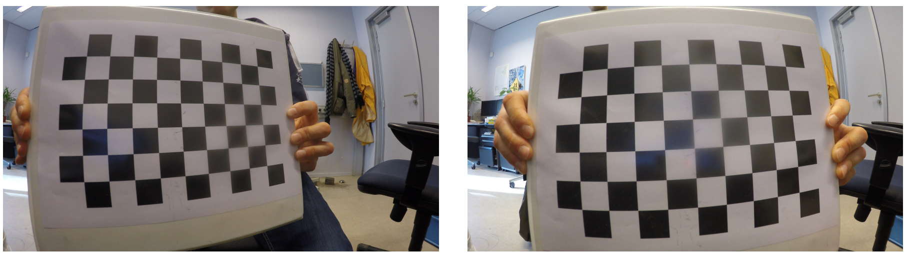

Figure 41: Two images of the checkerboard from a total set of 15

Remove fish eye distortion

```
clear all; close all

% Detect calibration pattern from set of checkerboard images
images =
 imageDatastore(fullfile(toolboxdir('vision'),'visiondata', ...
    'calibration','gopro'));
[imagePoints,boardSize] = detectCheckerboardPoints(images.Files);

% Generate coordinates for checkerboard squares with known dimensions
squareSize = 25; % millimeters
worldPoints = generateCheckerboardPoints(boardSize,squareSize);

% Use first image to get the size and obtain fisheye calibration
 parameters
I = readimage(images,1);
imageSize = [size(I,1) size(I,2)];
params = estimateFisheyeParameters(imagePoints,worldPoints,imageSize);

% Read GoPro images from file
before = imread('before_failure.png');
after = imread('after_failure.png');

% Correct images from fisheye distortion and write to graphics file
imwrite(undistortFisheyeImage(before,params.Intrinsics,'OutputView',...
    'full'),'before_failure_undist.png');
imwrite(undistortFisheyeImage(after,params.Intrinsics,'OutputView',...
    'full'),'after_failure_undist.png');

% Display original and corrected image
corrected = imread('after_failure_undist.png');
figure
imshowpair(after,corrected,'montage')
title('Original image (left) versus corrected image (right)')
```

Warning: Image is too big to fit on screen; displaying at 17%

Original image (left) versus corrected image (right)

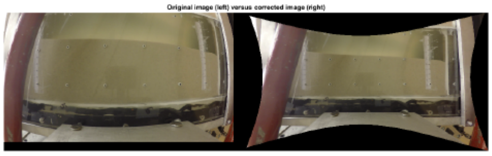

Compare images

```
% Read corrected images
fixed = imread('before_failure_undist.png');
moving = imread('after_failure_undist.png');

% Compare difference in images
difference = imshowpair(fixed,moving);
```

Warning: Image is too big to fit on screen; displaying at 33%

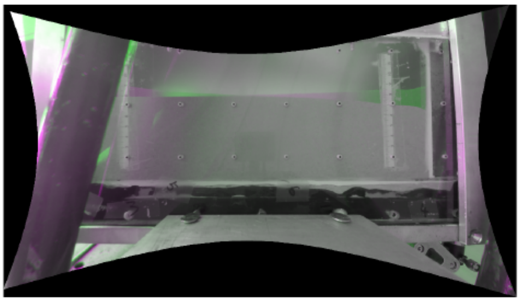

Published with MATLAB® R2017b

Figure 42: MATLAB script to correct fish eye distortion and to compare images

P Research proposal

This appendix contains the literature review and research description of the original research proposal. As most of the literature study appeared to be irrelevant, it was not adopted in the main report. The initial main objective concerning the effect of liquefaction flow slides on buried pipelines was eventually not feasible due to the large extent of preliminary experimental investigation. Centrifuge experiments with the installation of the buried pipeline will be performed and analysed in further research. Although the main objective and goals changed during the project and the initial approach was considered unsuccessful, all research questions have been answered in the report.

2. Literature review

2.1 Liquefaction flow slides

Soil liquefaction Soil liquefaction is a phenomenon which is generally defined as the loss of strength or stiffness of the soil under undrained conditions (Jefferies and Been, 2016). The accumulation of pore pressures lead to a decrease in effective stress, in extreme cases causing the soil to behave like a fluid. Liquefaction mainly occurs in loosely packed soils, as they have the tendency to contract when subjected to loading. The low permeability in soils prevents the volume decrease during shearing, resulting in a generation of excess pore pressures (Figure 43). Following the principle of effective stress (Terzaghi, 1925), the increase in pore pressure reduces the effective stress, which can lead to a total loss in strength, i.e. liquefaction (de Groot and Mastbergen, 2006).

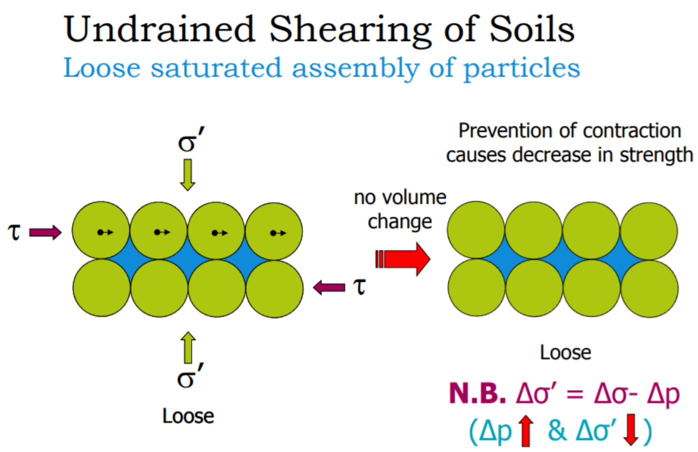

Figure 43: Undrained shearing of saturated loose soils (Jommi, 2016)

Three types of loading triggering liquefaction can be distinguished: monotonic, cyclic and dynamic loading (Poulos et al., 1985). Earthquakes are the most documented cause of liquefaction, which involves dynamic and cyclic loading conditions. Olson and Stark (2001) provided an analysis by dividing the case histories of liquefaction flow failure in three different categories: static- and deformation-induced and seismically induced failures. The interest of this research involves submarine flow failure under monotonic conditions, which is often referred to as static liquefaction.

Submarine landslides Landslides can be defined as the gravitationally driven mass movements at slopes due to shear failure. They can occur both on land and under water; in the latter case they are called submarine landslides. Hampton et al. (1996) provided an extensive overview of identified submarine landslides worldwide and the subaqueous environment in which they occur.

Two types of subaqueous slope instabilities are generally considered. Whitman (1985) made a distinction between flows and other types of landslides by introducing the terms ‘disintegrative’ and ‘non-disintegrative’ failure. While non-disintegrative failure involves settlements with intact geometry, disintegrative failure describes a flow mechanism with a total loss of shear strength and large deformations. Poulos et al. (1985) defined this latter type of failure as liquefaction. Additionally, he developed the principles of undrained steady-state strength and liquefaction potential.

Submarine flow slides due to liquefaction are characterized by the enormous volume of material being displaced and the very gentle slope after sliding (Silvis and de Groot, 1995). While liquefaction flow slides in man-made structures (embankments, tailing ponds, artificial islands, etc.) have occurred under various conditions, naturally induced flow slides have mainly been found in coastal loose sand deposits (Kramer, 1988). The reported flow slides were all situated near the shores of either fjords (Norway) or rivers (the Netherlands, Canada) and they were triggered by a fluctuation in water level.

In the footsteps of Koppejan et al. (1948), more recent research was performed on the occurrence of flow slides in the Netherlands. Silvis and de Groot (1995) presented a study of empirical field data and the geological environment in which flow slides occurred. Additionally, the Dutch approach of analysing the flow slide potential of underwater slopes was described. Following this procedure, a flow slide event requires three criteria (Stoutjesdijk et al., 1998):

- the soil needs to be sensitive to liquefaction,
- the slope must be sufficiently unfavourable (steep and high enough),
- an initiation mechanism is present to trigger liquefaction.

In other words, liquefaction flow slides will only occur in sufficiently high and steep slopes of loosely packed soil which are subjected to some kind of triggering mechanism.

Static liquefaction and potential instability Although the basic concept of static liquefaction is well understood, the exact micromechanical behaviour of the soil is not clear. Disagreement rises when it concerns the process why excess pore pressures can develop so quickly. One theory is based on the metastable grain arrangements, where sudden collapse of saturated voids cause the fast increase of pore pressures (Skopek et al., 1994; Chu et al., 2003; de Groot and Mastbergen, 2006; Ng, 2009; Askarinejad, 2013). This theory is supported by the concept of an instability line (IL), which corresponds to the maximum undrained shear strength which can be mobilized before strain softening (Lade, 1992). The location of the IL can be obtained by analysing the effective stress paths of triaxial tests under undrained conditions (Figure 44). The points of the shear strength yield surface or envelope for multiple tests are connected to form the IL.

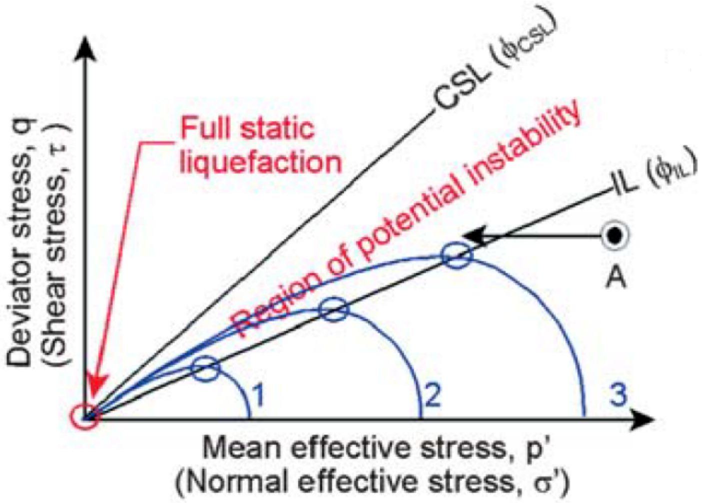

Figure 44: Undrained effective stress path and location of the instability line for a loose sand (Take et al., 2004)

The critical state line (CSL) represents the failure line obtained from drained triaxial tests. The zone between the IL and CSL is called the region of potential instability and samples will become unstable when the undrained effective stress path is situated in this zone (Lade and Pradel, 1990). The position of the IL is not unique; consolidated undrained triaxial tests were performed by Chu et al. (2003) to illustrate the dependency of the IL on void ratio and confining stresses. Where liquefaction is mostly related to undrained behaviour, Eckersley (1990) stated that the accumulation of excess pore pressures resulting in liquefaction is a consequence rather than the cause of a flow slide, and failure is initiated under drained conditions.

Further research on the phenomenon of potential instability includes the effect of silty fines, microstructure and depositional methods on the undrained behaviour of sands subjected to static liquefaction (Yamamuro and Wood, 2004; Yamamuro et al., 2008). Prior to this exploration, Yamamuro and Lade (1997) introduced a hypothesis containing four general types of undrained effective stress paths for loose silty sands with the same initial density under monotonic loading conditions. They consist of complete static liquefaction, temporary liquefaction, temporary instability and instability (Figure 45). Static liquefaction only occurs at low confining pressures as higher pressures densify the sample resulting in dilative behaviour. At very high pressures, however, the dilative behaviour is suppressed and particle crushing predominates the contractive behaviour (Lade et al., 1996). This theory only partially agrees with earlier research of Kramer and Seed (1988), who concluded that the liquefaction resistance increased with increasing relative density and confining pressures. This hypothesis was confirmed by Park and Byrne (2004), who stated that liquefaction phenomena can only be observed at shallow depths because they are being suppressed at higher confining pressures.

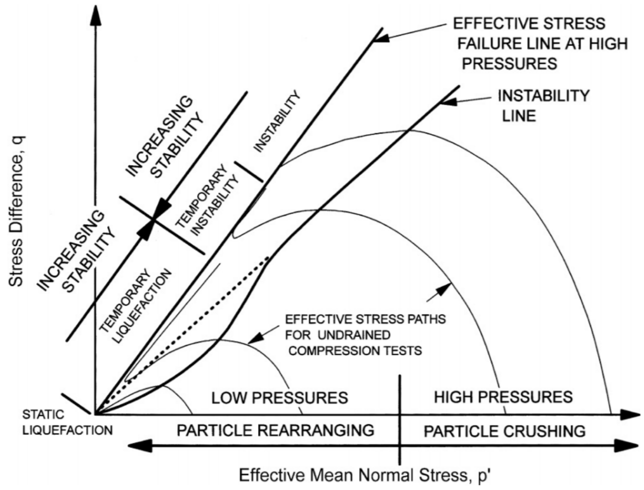

Figure 45: Four types of undrained effective stress paths for loose silty sands (Yamamuro and Lade, 1997)

The theory of metastable grain arrangements and regions of potential instability was subjected by Jefferies (2017), who described static liquefaction as a constitutive behaviour. The excess pore water pressure would be caused by plastic strains only without any collapse occurring. Jefferies and Been (2016) developed a framework of soil liquefaction based on a critical state approach with a state parameter relating the initial and current void ratios. The framework includes a soil model NorSand which captures the mechanics of liquefaction. Jefferies et al. (2012) and Lade (2012) discuss modelling of soil behaviour following the latter approach and the more conventional theory of void collapse.

Critical State Approach The critical state concept originates from research on dilatancy, which is the tendency of soils to change volume during shearing. Dense soils generally increase in volume (dilatation) while loose soils reduce in volume (contraction). Casagrande (1936) explored the relationship of both behaviours using a shear box test. It was found that dense and loose sand changed in volume until eventually the same void ratio was reached at large strains, i.e. the critical state void ratio.

The critical state void ratio depends on the mean effect stress, composing the critical state locus (CSL). The density of a soil, which is closely related to the void ratio, has a major influence on the behaviour in terms of contraction and dilatancy. Due to the wide range of possible densities, it is more favourable to consider the density as a state rather than a soil property. The critical state framework proposed by Jefferies and Been (2016) tends to distinguish the soil properties which are independent of the density (e.g. friction angle) and a current state (e.g. void ratio). The state parameter ψ has been defined, which is the difference of the current void ratio and critical void ratio (Figure 46). Soil behaviour can then be expressed as a function of this state parameter and soil properties unrelated to the density. In general, loose contractive soils have a positive ψ (decreasing void ratio) and dense dilatant soils have a negative ψ (increasing void ratio). The liquefaction potential is additionally evaluated by this state parameter following constitutive soil models.

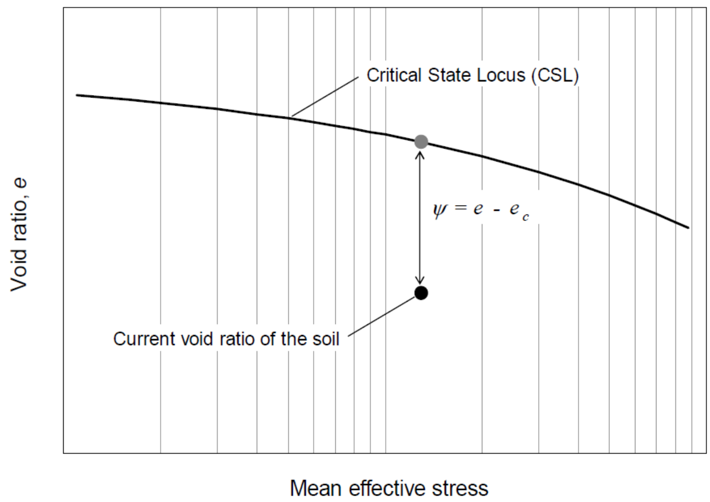

Figure 46: Diagram of void ratio against mean effective stress indicating the state parameter ψ (Jefferies and Been, 2016)

Buried pipelines subjected to soil liquefaction Research on the behaviour of buried pipelines in liquefiable soils mainly involves dynamic loading conditions. O'Rourke and Lane (1989) evaluated four case studies where damage to pipelines was caused by earthquakes. By using a soil/pipeline interaction model, it was shown how the orientations of pipelines relative to lateral spreading influences the deformations of the pipes. Due to the complexity of offshore site investigation, analysis of the behaviour of buried pipelines subjected to earthquakes is mainly performed by numerical models (Han et al., 2012; Roshan et al., 2010; Jafarzadesh et al., 2012). On the other hand, a few centrifuge experiments were performed in the past to evaluate the dynamic behaviour of pipes. Huang et al. (2014) used a beam centrifuge with shaking table to simulate a buried pipeline subjected to earthquake loading. It was concluded that the accumulation of excess pore pressures led to increasing buoyancy forces on the pipe resulting in uplifting movement. A similar centrifuge experiment and conclusion was described by Teymur and Madabhushi (2006). It is therefore clear that soil liquefaction due to earthquake loading may result in uplifting behaviour of buried pipelines. However, there exists a lack of knowledge when buried pipelines are subjected to liquefaction flow slides triggered by monotonic loading conditions.

2.2 Centrifuge modelling of static liquefaction

Many element tests (such as triaxial and shear box) have been executed to physically model the static liquefaction behaviour. However, Poulos et al. (1985) claimed that the liquefaction potential can only be determined when the shear strength and shear stresses are measured in situ. Sadrekarimi (2014) emphasized the influence of soil composition, fabric and sample disturbance to the undrained shear strength. The importance of the in situ shear strength asks for a representative model with similar geometry. The liquefaction tank at TU Delft is an example of a large scale model which is used to simulate submarine flow failure. Due to the limitations in space, however, only a thin layer of loose sand can be analysed. Since confining stresses play a crucial role in the instability potential of slopes, the geo-centrifuge is a useful device to simulate in situ stress conditions at larger depths. This section provides an overview of centrifuge experiments which have been performed to model static liquefaction and the scaling laws being applied.

Previous experiments Various centrifuge experiments have been performed to model the failure mechanism of static liquefaction. The possibilities of modelling static liquefaction on a submerged slope in the centrifuge were investigated by Boorder and van der Zon (2017). The used triggering mechanism consisted of a syringe system to locally increase the pore pressures by injecting fluid. It was concluded that a viscous pore fluid was necessary to cause liquefaction, as water would dissipate too quickly. Even with viscous fluid, however, full static liquefaction was not obtained. Phillips and Byrne (1995) designed a centrifuge model where a sandy slope saturated with viscous fluid was subjected to a rapid crest load. The surcharge was the triggering mechanism to cause static liquefaction and subsequent slope failure. Another important triggering mechanism which has been considered is rainfall infiltration (Take et al., 2004; Ng, 2009; Take and Beddoe, 2014; Askarinejad, 2013). The quick transition of unsaturated to saturated conditions can lead to large excess pore pressures and subsequent static liquefaction.

Due to the landslide risk and historical slope failures in Hong Kong, the triggering mechanism in layered granitic fill slopes was investigated. Following the work of Take et al. (2004), additional centrifuge modelling was performed to analyse the layering effect in a fill slope subjected to seepage flow (Kim et al., 2006). Results showed that pore pressures building up at the interface of the layers eventually caused shear failure. But although a slip surface could be clearly visualized, no liquefaction flow was obtained. Ng (2008, 2009) performed similar centrifuge tests by evaluating the effect of soil nails on loose granitic fill slopes. Both static and dynamic tests were executed, and a liquefaction flow was successfully generated by raising the ground water table.

Zhou et al. (2002) performed a series of centrifuge experiments to determine the critical gradient of underwater slopes consisting of silty sands and more granular sands, resulting in a range of 1:0.95 to 1:1 and 1:0.75 to 1:2 respectively. A remarkable conclusion states that the critical angle of the fine sand slope was not influenced by the g-level in the centrifuge.

Scaling laws and effects When a gravitational force of Ng is applied in the centrifuge, the height of the prototype is equivalent to N times the height of the model. The stresses and strains of the model with Ng centrifuge acceleration at the measured corresponding depths will be equal to those of the prototype. However, the distribution of vertical stresses is affected by the centrifuge radius. The caused error should be corrected by the under- and over-stress, resulting in a perfect agreement of stresses between model and prototype at two-third of the model's depth. For a broad outline of scaling laws and effects, the reader is referred to Taylor (1995). This section will be limited to the scaling factors with importance to modelling static liquefaction in the centrifuge.

A complicated issue regarding scaling effects concerns the dissipation time of excess pore pressures. A distinction is made between consolidation which includes seepage flow and dynamic events. Taylor (1995) proposed a factor of $1{:}N^2$ for seepage flow or diffusion and a scaling factor of $1{:}N$ for dynamic phenomena. He suggested a corrective strategy of slowing down the dissipation rate by increasing the fluid viscosity by factor N. The second method to compensate the time scale is reducing the particle size of the soil and subsequently its permeability. This is not preferred as the soil properties will change.

There exists some disagreement when it comes to the appropriate scaling law using viscous fluid when static liquefaction is involved. The most important research findings of this subject are addressed below.

- According to Askarinejad et al. (2014), the dissipation velocity of excess pore pressures will be N times faster in the model and the impact time of a particle falling by gravity will be $\sqrt{1/N}$ smaller. To reduce the dissipation time in the model a pore fluid which is $\sqrt{N}$ times more viscous than water should be used.
- In order to model submarine slope failures induced by seismic activity, Coulter (2005) used the pore fluid HPMC. He stated that a kinematic viscosity of 70 cSt is required for an acceleration of 70 g. However, half this viscosity was used to stimulate full saturation of the sand sample.
- For the centrifuge experiment with a crest load described by Phillips and Byrne (1995), an vegetable oil 50 times more viscous than water was used as pore fluid at 50 g. The scaling law applied was based on the consolidation coefficient, resulting in a fluid with a viscosity which was N times higher than water.
- Gue et al. (2010) developed scaling laws for submarine landslide flows in centrifuge modelling. The most remarkable difference is the scaling of flow distance, which is N^3 times larger for the prototype compared to the model, instead of the conventional N times. The suggested scaling laws were examined and confirmed by means of a mini-drum centrifuge.
- The scaling law for dissipation time during liquefaction of sand has been evaluated by Kim et al. (2006) by experimental comparison of the excess pore pressures generated in a 1-g and centrifuge test. A fluid with a N times higher viscosity than water was used in the centrifuge and the excess pore pressures were compared to the 1-g model. A scaling factor of N^m

was applied on the results of the 1-g model to match the dissipation times. The m values increased with depth and particle size, covering an overall range of 1.11 to 1.50. This means that the dissipation in a 1-g model with water is faster than in a centrifuge with a pore fluid being N times more viscous than water.

2.3 Laboratory investigation

Physical modelling requires a sample which is representative for the soil conditions on site. When a flow slide due to static liquefaction is being simulated, a couple of specific soil characteristics are required. The sand bed should consist of very loose saturated sand which is susceptible to liquefaction. This section gives a review of conventional and suitable preparation techniques, and methods which are used to evaluate the uniformity and degree of saturation of the obtained sand layer.

Sample preparation Undisturbed samples should be ideally retrieved in situ to be used for laboratory testing, for instance in triaxial cells. However, this can be practically impossible or very expensive, especially when it concerns submarine conditions. There exist several depositional methods to reproduce the sample artificially with the appropriate soil properties which can be found in the field. The most common depositional methods are moist tamping, wet or dry pluviation (also called dry funnel deposition and water sedimentation, respectively) and slurry deposition. A brief description of the advantages and drawbacks of these methods follows.

- Moist tamping is often used due to its ease and availability to reproduce very loose samples. The disadvantage is the obtained fabric of the material which does not correspond to the naturally found structure.
- Water sedimentation is useful for samples which have to be fully saturated without any consolidation effects due to capillary forces. The downside is the possible loss of sand fines and the impossibility to achieve a very loose state.
- Dry pluviation or dry funnel deposition is a fast and easy method to reproduce homogeneous dry samples. Different densities can be obtained by adjusting the drop height and tapping the split mold. Loose samples are nevertheless hard to achieve. Another disadvantage is the difficulty of measuring the volume changes during saturation.
- Slurry deposition was developed by Kuerbis and Vaid (1988) to tackle the particle separation problem in poorly graded sands. Homogeneous samples with silty sand can be obtained by this method (Yamamuro et al., 2008). The major drawback – similar to water sedimentation – is the range of achievable densities; wet depositional methods are not capable of producing loose specimens.

For an extensive overview of the elaborated and other sample preparation techniques, the reader is referred to Jefferies and Been (2016); Yamamuro and Wood

(2004); Yamamuro et al. (2008). The first mentioned paper also describes the influence of fabric on the behaviour of sand. Samples with the same soil properties but prepared with a different preparation method show dissimilar stress–strain curves.

Ueno (1998) reported a cooperative test to study the used techniques for the preparation of sand samples for centrifuge purposes. It was concluded that pluviation techniques are most popular and they are applied in the majority of the laboratories which cooperated. However, since the pluviation techniques cannot reproduce very loose sands, fluidization was introduced by de Jager and Molenkamp (2012) as a method to obtain homogeneous sand layers with a low density. These loose materials were required to model failures of static liquefaction in a tilting tank.

Fluidization Fluidization is the process of a fluid which passes upward through a granular material with such a velocity that the gravitational forces are balanced by the fluid drag. Subsequently, the grains will lose contact and flow inside the fluid; this is called fluidization (Davidson and Harrison, 1963; Davidson et al., 1985). Fluidization was introduced in the beginning of the twentieth century and was mainly used for applications in chemical engineering. After some decades it got related to geological phenomena such as volcanic and subaqueous occurrences, where exsolved gases were involved. Allen (1984) outlined the fluidization mechanism in terms of sedimentary structures, as water currents can fluidize the sedimentation beds on the sea floor.

As a fluidized sand bed is supposed to be homogeneous and very loose, it fulfils the conditions to trigger static liquefaction under a slope. Adding the fact that such sand layers can actually be present at subaqueous slopes, fluidization was introduced as a technique for sample preparation (de Jager and Molenkamp, 2012). The fluidization system was initially tested on samples prepared for triaxial testing and later it was copied on a large scale to the liquefaction tank at TU Delft (Krapfenbauer, 2016; de Jager et al., 2017). The properties of saturated loose sand samples prepared by fluidization were reported by Noriega (2015). The uniformity of the obtained sand bed in both a permeameter and the liquefaction tank was investigated by Lamens (2015) in terms of porosity and particle segregation.

According to Allen (1984), a similar fluidization process which he calls stationary fluidization – as there is only vertical movement of the grains – can also occur in natural sedimentary deposits. Since the geometry and flow conditions are comparable to the above described fluidization system, the presented minimum fluidization velocity can be compared. The obtained critical velocity is based on the pressure drop which reaches a constant value when the sand layer does not expand any longer. Equalizing the immersed bed weight to the pressure drop combined with the Carman-Kozeny equation, a range of fluidization velocities in function of particle diameter is obtained (Figure 47).

Uniformity sand layer Various methods have been developed to evaluate the homogeneity of a sand bed. Choi et al. (2010) used cone penetration tests, shear wave velocity and density measurement of small molds to analyse the uniformity of granular samples prepared by an advanced rainer system. The latter method

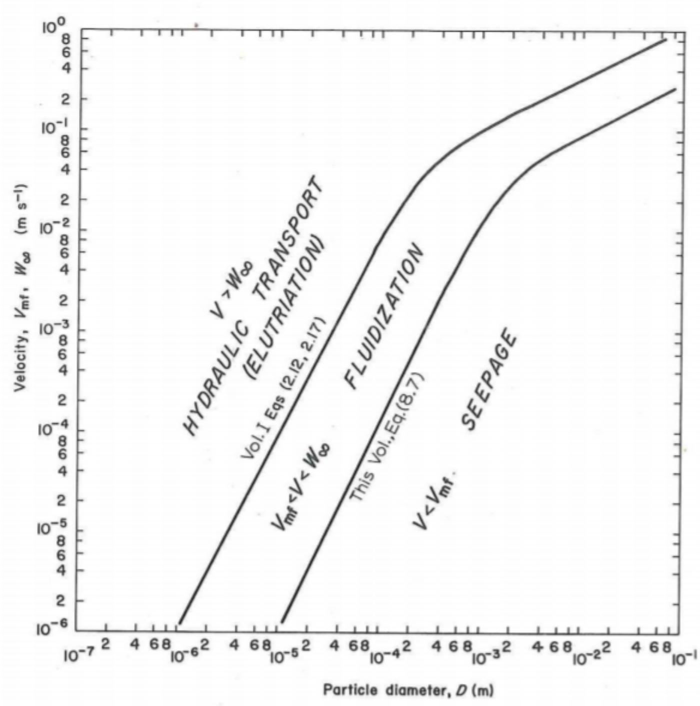

Figure 47: The critical fluidization velocity of quartz spheres in water (Allen, 1984)

is suitable for pluviation techniques as the sand is deposited from the top. For the cone penetration test, Puppala et al. (1995) proposed a minimum diameter ratio between the cone and chamber boundaries of 40. Bender elements were installed for the shear wave velocity to back-calculate the relative density and evaluate the vertical homogeneity of the specimen.

Degree of saturation Modelling a submarine landslide subjected to static liquefaction necessitates a sample which is 100% saturated. Making sure the degree of saturation equals one is of crucial importance because unsaturated behaviour influences the event. As the sand layer is fluidized during a certain period, it is infeasible to calculate the degree of saturation by the water volume. Takahashi et al. (2006) evaluated the saturation of sandy ground by using P-wave velocity. This method led to the conclusion that samples prepared by both the vacuum or gas and vacuum technique were fully saturated.

3. Research description

3.1 Problem definition

Static liquefaction of submarine slopes is a phenomenon which is still not completely understood. Element testing and physical models on both large scale and in the centrifuge have been performed to analyse the failure mechanism. At the Technical University of Delft a large tank has been built with a tilting mechanism to trigger static liquefaction on a submerged slope. Although the tank was capable of reproducing liquefaction flow slides (de Jager et al., 2017), the thickness of the sand layer was limited by the dimensions of the tank. Due to the stress-dependent behaviour of soils, the stress–strain graphs can vary significantly by the depth. It is therefore important to reproduce the confining stresses which are found in nature. Research has shown that the slopes of scour holes at the Eastern Scheldt Barrier can reach heights of 20 metres. As it would be impossible to model a representative soil layer at large scale, this can only be done by centrifugal acceleration. Centrifuge modelling of a liquefaction flow slide triggered by a tilting mechanism has never been performed.

3.2 Research goal and questions

The main objective of this research project is to evaluate the stresses acting on a buried pipeline when a submarine landslide occurs due to static liquefaction. This analysis is performed by means of centrifuge modelling to obtain realistic in situ confining stresses. The flow slide will be triggered by a tilting mechanism to obtain various sloping angles in the saturated sand layer.

In order to achieve the main goal, the project can be split up in segments by introducing the research questions. One aspect of the questions concerns the physical aspects of centrifugal experiments, such as the sample preparation and measurements. The main facet of the investigation consists of the soil behaviour when a saturated loose sand is subjected to high confining stresses followed by a tilting mechanism.

1. **Does the sample preparation technique of combining vacuum saturation and fluidization result in a fully saturated homogeneous layer?**

   The most important features for the sand sample are uniformity and full saturation. Although fluidization led to a uniform sand bed in the large scale liquefaction tank, it is unsure whether the system on small scale in the strongbox will give similar results. Attention should furthermore been paid on the uniformity of the consolidation process when fluidization terminates. To represent a subaqueous deposited layer, the sand has to be fully saturated for accurate results and to avoid any effects of unsaturated soil behaviour.

2. **How can the relative density be measured accurately during centrifuge modelling?**
   Previous research has shown that instability and liquefaction failure is strongly related to the void ratio and consequently relative density. Artefacts in experimental results were caused by the reference of (initial) void ratio; increasing the confining stresses under drained conditions will lead to consolidation and increase in relative density. It is therefore important to measure the relative density accurately during in-flight conditions.

3. **How will higher confining stresses affect the soil behaviour and static liquefaction mechanism?**
   Disagreement exists in the analysis of loose soils subjected to high confining pressures. Where some authors state that the liquefaction potential

decreases when the confining pressures increase (Kramer and Seed, 1988), others brought forward that the suppressed dilative behaviour and particle crushing will lead to instability (Lade et al., 1996).

4. **What is the effect of the tilting rate?**
   Static liquefaction is usually related to undrained behaviour as pore pressures accumulate due to a lack of dissipation. The limitation of seepage is assumed to depend on the tilting rate. Additionally, it will be interesting to observe whether the rate to cause liquefaction flow is comparable to the experiment performed by the large scale tilting tank.

5. **What is the viscosity of pore fluid which needs to be used in order to meet the appropriate scaling laws?**

   Due to the acceleration forces in the centrifuge, pore fluid will dissipate much faster than under 1g conditions. However, realistic pore pressures play a crucial role in liquefaction behaviour of soils. To overcome this issue a pore fluid with higher viscosity needs to be used. Nevertheless, there is a lack in consistency when it concerns the appropriate scaling law for seepage of pore fluid.